UCLA
UCLA Previously Published Works

Title

A Heat Transfer Model for Graphene Deposition on Ni and Cu Foils in a Roll-to-Roll Plasma Chemical Vapor Deposition System

Permalink

https://escholarship.org/uc/item/1t53z9xr

Journal

Journal of Heat Transfer, 143(10)

ISSN

0022-1481

Authors

Alrefae, Majed A
Fisher, Timothy S

Publication Date

2021-10-01

DOI

10.1115/1.4051505

Peer reviewed

A Heat Transfer Model for Graphene Deposition on Ni and Cu Foils in a Roll-to-roll Plasma Chemical Vapor Deposition System

Majed A. Alrefae[*]
School of Mechanical Engineering and Birck Nanotechnology Center
Purdue University
West Lafayette, IN 47907

Timothy S. Fisher[†]
Mechanical and Aerospace Engineering Department
University of California
Los Angeles, CA 90095

ABSTRACT

High-throughput production is a major bottleneck for integration of graphene-based technologies in existing and future applications. Here, a semi-empirical heat transfer model is developed to optimize large-scale deposition of graphene on Ni and Cu foils in a roll-to-roll plasma chemical vapor deposition (CVD) system. Temperature distributions in Ni and Cu foils during deposition are recorded with in situ temperature measurements using near-IR optical emission spectroscopy. The model indicates that foil movement significantly affects the temperature distribution and the cooling rate of the foil. Consequently, graphene growth on Cu is limited to lower web speeds for which the foil temperature is higher, and the residence time in the plasma is longer. On the other hand, graphene can be deposited on Ni at relatively higher web speeds due to moderately high diffusion rate of carbon in Ni and increased cooling rates up to 20 K/s with higher web speed. Critical limitations in the production rates of graphene using roll-to-roll CVD process exist due to significant effects of web speed on the temperature distribution of the substrate. The thermal analysis approach reported here is expected to aid in enhancing the throughput of graphene production in roll-to-roll CVD systems.

1 Introduction

Roll-to-roll (R2R) manufacturing techniques have been implemented to mass-produce graphene, which is a two - dimensional carbon material [1–5]. Previous reports have demonstrated the successful application of R2R processes for graphene growth on Cu foil using thermal furnace chemical vapor deposition (CVD) [6–8], Joule heating CVD [9] and plasma CVD [10, 11]. The extensive use of Cu substrates for large-scale deposition of graphene is due to the low cost of Cu, the self-limiting growth of graphene on Cu and the ease of graphene transfer from Cu to other substrates [12]. Because of low carbon solubility in Cu, graphene growth on Cu is driven by surface catalytic-like reactions that occur at high temperatures (approx. 1200 K) [13]. Consequently, in R2R processes the web speed controls the growth of graphene because the substrate temperature depends significantly on the duration of exposure to a high-temperature environment [7, 11, 14].

Alternatively, Ni substrates have been widely used for large-area deposition, from mono- to few-layer graphene and thin graphite [15–20]. Graphene growth on Ni is initiated by the decomposition of methane (CH_4) (or another hydrocarbon source) to intermediate carbon species at temperatures higher than 900 K. These carbon species dissolve in the Ni substrate to form metastable nickel carbides resulting from relatively high carbon solubility in Ni [21]. Upon cooling, elemental carbon precipitates and segregates on the Ni surface due to decreased carbon solubility as the substrate cools. As a result, graphene

---

[*]Current address: Yanbu Industrial College, Yanbu Industrial City 41912, Saudi Arabia. Email: majed.alrefae@outlook.com, Tel: +966 53-919-1994.
[†]Corresponding author, Email: tsfisher@ucla.edu, Tel: +1 310-206-8113.

with different qualities and thicknesses emerge on the Ni surface, depending on the cooling rate [15]. However, large-scale production of graphene on Ni using R2R CVD methods has not been previously reported.

Following the work of Yu et al. [15], several studies have considered the effects of cooling rate on graphene deposition with Ni substrates, as summarized in Table S-1 in the Supporting Information. Previous reports have categorized the cooling rates as either slow or fast, or according to an intermediate rate between the two. These cooling rates were primarily derived from thermocouple measurements of the substrate holder, and not directly from the substrate. Moreover, a constant cooling rate over time is unlikely due to the non-linearity of convection and radiation processes associated with local gas flow and chamber walls. Consequently, the cooling rates associated with the successful growth of few-layer graphene are inconsistent in prior literature as evident from Table S-1. Therefore, the absence of a detailed heat transfer analysis of Ni substrate hinders the potential of its utilization for scalable graphene production.

In order to control large-scale R2R processes for graphene on Ni and Cu foils, a detailed understanding of the temperature distribution during the R2R process is necessary. The temperature profile of the substrate during R2R processing can be determined from analysis of a moving plate/web in a fluid medium. Heat transfer and fluid flow with a moving plate in a quiescent fluid medium have been modeled previously using boundary layer theory [22, 23]. However, heat conduction within the moving plate itself was not included in these earlier studies because the plate was assumed to be isothermal. The temperature distribution of the moving plate/web was determined in later reports either by solving the coupled fluid and plate heat diffusion equations [24–26], or by using a prescribed heat transfer coefficient and solving the heat diffusion equation in the plate alone [27–31]. The temperature of the moving plate was found to depend on web speed, material properties and flow conditions.

Here, we focus on the impact of heat transfer on the temperature distributions in Ni and Cu foils, and their relationship to graphene growth in a R2R plasma CVD system. The heat transfer model includes convection boundary conditions for quiescent flow and plasma gas, radiation exchange with the chamber wall and the plasma electrodes, and fin-type conduction and advection associated with the moving foil. The heat transfer model is informed by non-intrusive *in situ* temperature measurements of the substrate. Moreover, Raman spectroscopy and scanning electron microscopy (SEM) are utilized to assess graphene quality and uniformity as functions of web speed to determine optimal conditions for continuous R2R deposition of graphene on Ni and Cu foils. The effects of web speed on the quality and uniformity of graphene on Ni and Cu foils are correlated to the changes in the temperature profile of the substrate with web speed. The heat transfer analysis and graphene characterization methods reported in this work advance the possibility of mass production of graphene on Ni and Cu substrates.

2 Experimental Setup

The R2R plasma CVD system used here was custom-designed to deposit graphene on a variety of flexible substrates [11, 14, 32]. As-received nickel (201 annealed nickel, 76.2 μm (or 0.003 inch) thick and 25.4 mm (or 1.00 inch) wide purchased from All Foils Inc.) or copper (110 annealed copper, 76.2 μm (or 0.003 inch) thick and 25.4 mm (or 1.00 inch) wide purchased from Basic Copper Inc.) was placed in a top, free-moving winder, passed through a plasma region where carbon film was deposited because of the high gas temperature in the plasma, and finally collected at the bottom driving winder (Fig. 1). Initially, the system was evacuated to less than 0.1 mbar; then a gas mixture of 50:50% H_2:Ar by volume was introduced at 7 mbar to ignite the plasma at a power of 500 W. Thereafter, pressure and power were increased after a warm-up period to 15 mbar and 850 W, respectively, and CH_4 was added to the H_2/Ar mixture for graphene growth. The flow rates of Ar, H_2 and CH_4 during graphene growth were 150, 610 and 260 standard cubic centimeters per minute (sccm), respectively.

Experiments were conducted at a constant plasma power of 850 W and a fixed gas pressure of 15 mbar. Power was supplied to two parallel electrodes to generate a capacitively coupled rf plasma at a frequency of 80 kHz. The electrodes, which are made of graphite, had rectangular shapes with lengths of 12.5 cm and widths of 5.0 cm. The distance between the electrodes was fixed at 4.5 cm, and the distance between the right electrode and the foil was 1.5 cm (Fig. 1). The substrate moved in the plasma region at web speeds of 0, 50 and 150 mm/min which were assessed during the experiments with a speed uncertainty of 10%. The residence times for the null web speed were 21.3 and 17.0 min for Ni and Cu foils, respectively.

After the experiment, Raman spectroscopy was used to quantify the quality of graphene deposited on the foil without transfer of the carbon film. Raman spectra were measured using LabRAM Horiba Ltd. Raman spectrometer with a laser excitation of 532 nm and 100x magnification. Also, scanning electron microscopy (SEM) using S-4800 from Hitachi Corp. was utilized to visualize carbon films on the foil with a 1 kV accelerating voltage at various magnifications.

The foil temperature in the plasma region was measured directly from its radiative emission using optical emission spectroscopy (OES). The emission was collected and collimated using 50.8 mm diameter lenses, focused on a fiber optic held by a fixture that allowed motion to a precise location along horizontal and vertical axes using Zaber translation stages. The spatial resolution of the emission measurement was estimated to be approximately 2 mm. The fiber optic transmitted the emission to a spectrometer (Princeton Instruments, Acton SP-2756) which has a grating of 1800 G/mm and a CCD camera
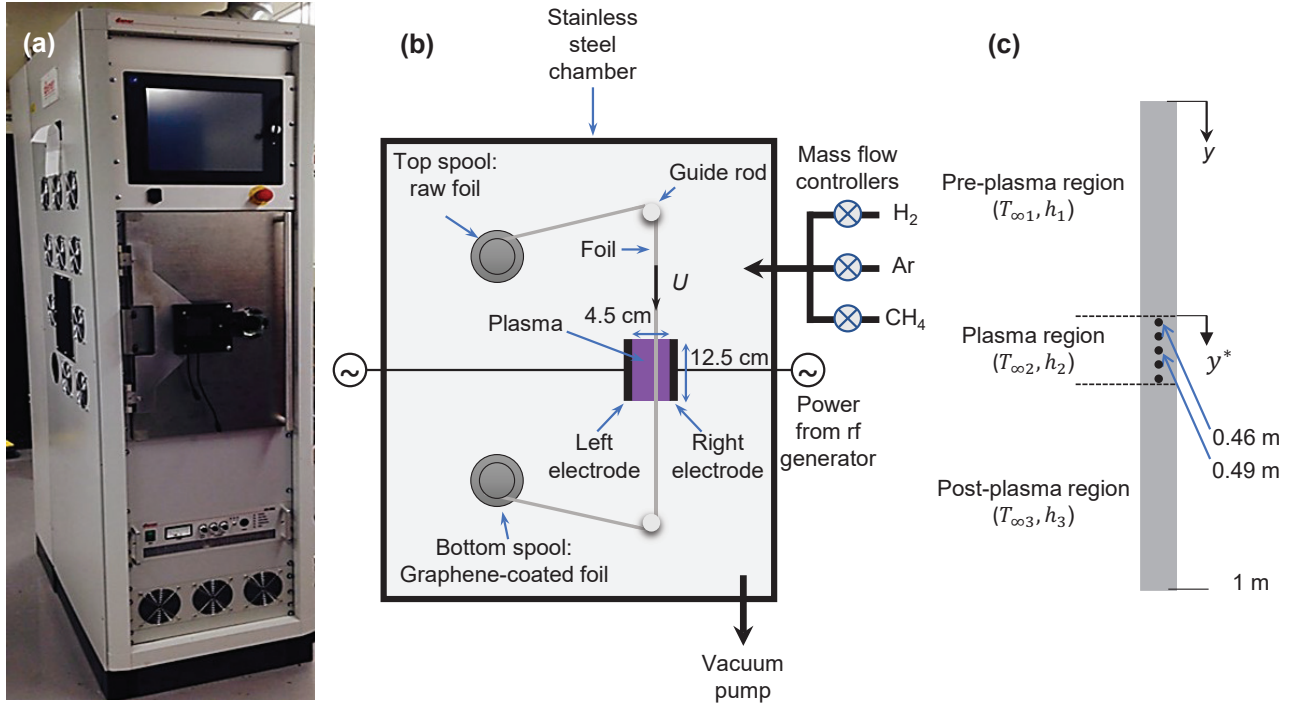
Fig. 1: (a) The R2R plasma CVD system. (b) Schematic of the R2R plasma CVD system. (c) Side view of the foil illustrating the three regions with their corresponding temperatures and heat transfer coefficients.

(Princeton Instruments, PIXIS 256E). The spectrometer was calibrated in the range of 670-850 nm using a mercury light source.

The measurement of emission was controlled by LightField software (from Princeton Instruments) to acquire high-resolution spectral data over a broad wavelength range. Equally spaced spectra of about 15 nm increments were measured individually by rotating the grating to cover the 670-850 nm range. The discontinuity between each measured spectral band that arises from changes in grating diffraction efficiency with wavelength was corrected by calibrating using an intensity-calibration light source. The calibration of intensity plays an important role in accurately measuring the spectra from the substrate over the 670-850 nm range.

The emission intensity from the substrate (I) can be fitted to Planck's distribution, which depends on temperature (T) and wavelength (λ) as [33]:

$$I(\lambda, T) = A + \frac{B}{\lambda^5} \frac{1}{exp(\frac{hc}{\lambda k_B T}) - 1} \tag{1}$$

where k_B is Boltzmann's constant (1.381×10^{-23} J/K), A is the linear offset of the spectrum, and B is a constant that represents Planck's constant ($h = 6.626 \times 10^{-34}$ J.s), the speed of light ($c = 2.998 \times 10^8$ m/s), the foil emissivity and the contribution from the optical emission setup as described in [34]. Because the emissivity of Ni and Cu foils are nearly constant in the 670-850 nm wavelength range, foils are assumed to be gray surfaces with emissivity values of 0.14 and 0.04, respectively, at 1000 K [33]. The detector and grating responses as functions of wavelength were included in the intensity calibration. The temperature (T) and the constants (A and B) were found from a nonlinear least-squares fitting method using Matlab as described in the Supporting Information. The contributions from species emission were filtered out; thus, only the baseline of the spectrum was included in the fitting, as shown in Fig. S-1 in the Supporting Information.

3 Heat Transfer Model

The ability to measure the foil temperature at various vertical points along the plasma region allows for refinement and validation of a heat transfer model that considers a 1-meter long foil starting from the top spool and ending at the bottom spool (Fig. 1(b)). During the R2R CVD process, the foil encounters three regions: pre-plasma, plasma, and post-plasma as illustrated in Fig. 1(c). Convective flow, which is driven primarily by buoyancy, is assumed to be isothermal and uniform in each of the three regions. The gas temperatures in the pre- and post-plasma regions ($T_{\infty 1}$ and $T_{\infty 3}$, respectively) are assumed

to be 313 K, as measured by a thermocouple. On the other hand, the gas temperature in the plasma region ($T_{\infty2}$) is assumed to be 1100 K as estimated from the rotational temperature of H_2 using OES [35] (Fig. S-2 in the Supporting Information). Furthermore, the temperatures of the right and left electrodes (as indicated in Fig. 1(b)) are 892 and 870 K, respectively, as determined from their emission spectra in the same manner described for the foil temperature in Eq. 1.

The heat transfer coefficients in the three regions are derived from fitting the model to the measured Cu foil temperatures (Fig. S-3 in the Supporting Information). The coefficients h_1 and h_3 are similar and fixed at 5 W/m^{2}K, and we found in preliminary analyses that the results are relatively insensitive to these values as long as the coefficient is relatively small. By corollary, the present model and measurements clearly lack the fidelity to capture the complex fluid-thermal behavior that would be required to refine this assumption. The heat transfer coefficient in the plasma region (h_2) is used as a fitting parameter of the model to match the experimentally measured foil temperatures as explained later in this section.

In addition, a steady-state flow condition is assumed in the analysis because chamber wall temperatures reached a steady state, and the foil moved at a constant prescribed web speed. Because of the small foil thickness (δ) and width (w), which are 76.2 μm and 25.4 mm, respectively, the Biot number is below 0.01. Therefore, a one-dimensional fin model is developed to solve for the substrate temperature along the foil length using analytical and numerical approaches as explained below.

3.1 Derivation of the Analytical Heat Transfer Model

The analytical model treats the three regions (i.e., pre-plasma, plasma and post-plasma regions) separately, and the final foil temperature distribution is found by combining the three regions with appropriate boundary conditions. To simplify the analysis of boundary conditions, the coordinate system is shifted to start from the plasma region (i.e., $y^* = y - 0.4375$ m) as shown in Fig. 1(c). Applying an energy balance in a control volume within region i (see Supporting Information and Fig. S-4) results in the following differential equation:

$$\frac{d^2\theta_i}{(dy^*)^2} - a\frac{d\theta_i}{dy^*} - m_i\theta_i = 0 \tag{2}$$

where $\theta_i = (T - T_{\infty,i})$, $a = \frac{\rho U c_P}{k}$ and $m_i = \frac{2h_i}{k\delta} + \frac{(h_{rad,Li}+h_{rad,Ri})}{k\delta}$. The regions $i = 1, 2$, and 3 correspond to the pre-plasma, plasma, and post-plasma locations, respectively. Also, ρ is the density of the foil (8933 and 8900 kg/m^3 for Cu and Ni, respectively [33]), and U is the web speed.

To obtain closed solutions, we assume constant material properties for the post-plasma region with values of specific heat (c_P) and thermal conductivity (k) taken from [33] at $T_{\infty3}$ (i.e., 313 K). Here, h_3 is the convective heat transfer coefficient in the post-plasma region with a value of 5 W/m^{2}K as explained above. The convection from both sides of the foil is assumed to be equal. Also, $h_{rad,R3}$ and $h_{rad,L3}$ are the linearized radiative transfer coefficients from the right and left sides of the foil (assumed equal in this region), respectively, to the chamber wall in the post-plasma region (refer to the Supporting Information for more details of the derivation). Thus, the general solution of the differential equation (Eq. 2) takes the form:

$$\theta_3(y^*) = C_1 exp\left(\frac{1}{2}y^*(\sqrt{a^2+4m_3}+a)\right) + C_2 exp\left(-\frac{1}{2}y^*(\sqrt{a^2+4m_3}-a)\right) \tag{3}$$

where C_1 and C_2 are constants that are determined with appropriate boundary conditions. Note that y^* is the shifted y-coordinate written as $y^* = y - 0.4375$ m to simplify the solutions of C_1 and C_2.

An energy balance analysis in the pre-plasma region leads to the differential equation of Eq. 2 with $\theta_1 = (T - T_{\infty1})$, and $m_1 = \frac{2h_1}{k\delta} + \frac{2h_{rad,R1}}{k\delta}$. Similar to the post-plasma region, h_1 is 5 W/m^{2}K, and $h_{rad,R1}$ can be derived similarly to $h_{rad,R3}$. Also, specific heat (c_P) and thermal conductivity (k) values are taken at $T_{\infty1}$ (i.e., 313 K). Thus, the general solution of the temperature distribution in the pre-plasma region takes the form:

$$\theta_1(y^*) = C_3 exp\left(\frac{1}{2}y^*(\sqrt{a^2+4m_1}+a)\right) + C_4 exp\left(-\frac{1}{2}y^*(\sqrt{a^2+4m_1}-a)\right) \tag{4}$$

The energy balance in the plasma region encompasses heating from the plasma constituents. For instance, heat transfer from the plasma accounts for substrate heating from electrons, neutrals, and ions, as well as surface reactions [36]. These heat fluxes depend on electron temperature, electron number density, reaction rates, and gas temperature, which are unknown and challenging to measure (except for the plasma gas temperature, $T_{\infty2}$). Nevertheless, the heat fluxes from plasma processes can be lumped into an effective heat transfer coefficient (h_2) multiplied by the temperature difference between the foil and plasma gas ($T - T_{\infty2}$). Hence, h_2 is used as a fitting parameter of the model to match foil temperature measurements, resulting

4

in values of 55, 30, and 29 W/m²K for Cu, and 36, 30, and 28 W/m²K for Ni at 0, 50, and 150 mm/min, respectively. For both Cu and Ni, h_2 decreases with increased web speed indicating lessened interactions of the plasma gas with the foil.

Furthermore, radiation exchange between the foil and the two electrodes in the plasma region is derived in the Supporting Information. The linearized radiative transfer coefficients from foil to the right and left electrodes are included in $h_{rad,R2}$ and $h_{rad,L2}$, respectively. Therefore, the final differential equation for the foil temperature in the plasma region takes the form of Eq. 2, with $\theta_2 = (T - T_{\infty 2})$, and $m_2 = \frac{2h_2}{k\delta} + \frac{h_{rad,R2}}{k\delta} + \frac{h_{rad,L2}}{k\delta}$. Also, the electrode temperatures are assumed to equal $T_{\infty 2}$ (only in the analytical model) to combine the convective and radiative terms in m_2 and to simplify the differential equation. Specific heat (c_P) and thermal conductivity (k) values in the plasma region are obtained at a fixed temperature of $T_{\infty 2}$ (i.e., 1100 K). Thus, the general solution of the temperature distribution in the plasma region is:

$$\theta_2(y^*) = C_5 exp\left(\frac{1}{2}y^*\left(\sqrt{a^2 + 4m_2} + a\right)\right) + C_6 exp\left(-\frac{1}{2}y^*\left(\sqrt{a^2 + 4m_2} - a\right)\right) \qquad (5)$$

The general solutions of the temperature distributions (Eq. 3 to Eq. 5) have six constants that can be evaluated by applying the following boundary conditions:
(a) Infinite fin boundary condition: $\theta_3(y^* \to \infty) = 0$, leading to $C_1 = 0$ in Eq. 3.
(b) Infinite fin boundary condition: $\theta_1(y^* \to -\infty) = 0$, leading to $C_4 = 0$ in Eq. 4.
(c) Temperature continuity at the interface of the pre-plasma and plasma regions: $\theta_1(y^* = 0) + T_{\infty 1} = \theta_2(y^* = 0) + T_{\infty 2}$.
(d) Heat conduction flux continuity at the interface of the pre-plasma and plasma regions: $k_1 \frac{d\theta_1(y^*=0)}{dy^*} = k_2 \frac{d\theta_2(y^*=0)}{dy^*}$.
(e) Temperature continuity at the interface of the plasma and post-plasma regions: $\theta_2(y^* = L) + T_{\infty 2} = \theta_3(y^* = L) + T_{\infty 3}$.
(f) Heat conduction flux continuity at the interface of the plasma and post-plasma regions: $k_2 \frac{d\theta_2(y^*=L)}{dy^*} = k_3 \frac{d\theta_3(y^*=L)}{dy^*}$.
where L is the length of the plasma region (i.e., the length of the electrodes, $L = 0.125$ m). A coordinate transformation simplifies the form of the constants C_2, C_3, C_5 and C_6, which are found by solving the set of linear equations from boundary conditions (c)-(f). Final expressions for the constants C_2, C_3, C_5 and C_6 are included in the Supporting Information.

The analytical solution for the foil temperature distribution during the roll-to-roll process is:

$$T(y^*) = T_{\infty 1} + C_3 exp\left(\frac{1}{2}y^*\left(\sqrt{a^2 + 4m_1} + a\right)\right) \qquad \text{for } -0.4375 \leq y^* < 0 \qquad (6)$$

$$T(y^*) = T_{\infty 2} + C_5 exp\left(\frac{1}{2}y^*\left(\sqrt{a^2 + 4m_2} + a\right)\right) + C_6 exp\left(-\frac{1}{2}y^*\left(\sqrt{a^2 + 4m_2} - a\right)\right) \qquad \text{for } 0 \leq y^* \leq L$$

$$T(y^*) = T_{\infty 3} + C_2 exp\left(-\frac{1}{2}y^*\left(\sqrt{a^2 + 4m_3} - a\right)\right) \qquad \text{for } L < y^* \leq 0.5625$$

Note that Eq. 6 reverts to the infinite fin model when the web speed is set to zero (i.e., when $a = 0$) [33].

3.2 Derivation of the Numerical Heat Transfer Model

The temperature distribution of the foil can also be solved numerically to incorporate non-linearities in radiation heat transfer and temperature-dependent material properties. An energy balance in the control volume of the foil (Fig. S-4) considering conduction (q_N and q_S), advection ($(w\delta\rho U c_P T)_N$ and $(w\delta\rho U c_P T)_S$), convection (q_{conv}), and radiation ($q_{rad,R}$ and $q_{rad,L}$) leads to:

$$q_N + q_S + w\delta(\rho U c_P T)_N = w\delta(\rho U c_P T)_S + 2dq_{conv} + dq_{rad,R} + dq_{rad,L} \qquad (7)$$

The temperature profile is assumed to vary linearly between cell centroids [37]. Hence, heat fluxes from the top and bottom cells (i.e., q_N and q_S, respectively) are found by: $q_N = \frac{kw\delta}{(\Delta y)}(T_{j-1} - T_j)$ and $q_S = \frac{kw\delta}{(\Delta y)}(T_{j+1} - T_j)$ where Δy is the cell size. Also, T_j, T_{j+1} and T_{j-1} are the central cell (j), its south ($j+1$) and north ($j-1$) neighbor cell temperatures, respectively (Fig. S-4). Temperatures T_N and T_S of the neighboring cells, using the central differencing discretization scheme, are given by $T_N = \frac{(T_{j-1}+T_j)}{2}$ and $T_S = \frac{(T_{j+1}+T_j)}{2}$. The convection term is written as $q_{conv} = h_i w(\Delta y)(T_j - T_{\infty i})$ for $i = 1, 2$ and 3, representing the pre-plasma, plasma and post-plasma regions, respectively. The factor of 2 in front of q_{conv} in Eq. 7 accounts for convection from both sides of the foil, which is assumed to be symmetric. Radiation from the foil to the electrode and to the chamber wall on the right and left sides (i.e., $q_{rad,R}$ and $q_{rad,L}$, respectively) are derived in the Supporting Information.

The final equation is:

$$a_j T_j = a_{j-1} T_{j-1} + a_{j+1} T_{j+1} + b \qquad (8)$$

$$a_j = 2\frac{k\delta}{(\Delta y)} + 2h_i(\Delta y) + 2\frac{4\varepsilon\sigma(\Delta y)(T_j^*)^3}{1-\varepsilon}$$

$$a_{j-1} = \frac{k\delta}{(\Delta y)} + 0.5(\rho U c_P \delta)$$

$$a_{j+1} = \frac{k\delta}{(\Delta y)} - 0.5(\rho U c_P \delta)$$

$$b = 2h_i(\Delta y)T_{\infty i} + \frac{\varepsilon(\Delta y)\left(J_{foil-R}^* + 3\sigma(T_j^*)^4\right)}{1-\varepsilon}$$

$$+ \frac{\varepsilon(\Delta y)\left(J_{foil-L}^* + 3\sigma(T_j^*)^4\right)}{1-\varepsilon}$$

where i = 1, 2 and 3 for the pre-plasma, plasma and post-plasma regions, respectively. Also, ε is the emissivity of the foil and σ is the Stefan-Boltzmann constant (5.67×10^{-8} W/m^{2}K^4). A mesh-independence study (Fig. S-5) led to a cell size (Δy) of 10^{-4} meter (i.e., the number of cells is 10,000). T_j^* denotes the central cell temperature from the previous iteration. Similarly, J_{foil-R}^* and J_{foil-L}^* are the radiosities of the right and left foil surfaces, respectively, from the previous iteration.

An iterative scheme solution is implemented in Matlab to update temperature-dependent properties (i.e., c_P and k), radiosity (J_{foil-R}^* and J_{foil-L}^*) and temperature from the previous iteration (T_j^*) in Eq. 8. The solution is assumed to be converged when the relative temperature change between current and previous iterations is less than 10^{-4}.

Both analytical and numerical models have identical temperature profiles when the radiation heat transfer is neglected (Fig. S-6). However, the analytical model with the inclusion of radiation heat transfer overpredicts the foil temperature in the plasma region due to the linearization of the radiation terms. Thus, the results from the analytical solution provide qualitative insights into the heat transfer processes in the foil, but the numerical model, which treats the radiation exchange and temperature-dependent properties more thoroughly, is used to find the Ni and Cu foil temperature distributions in the remainder of this work.

4 Results and Discussion
4.1 Estimation of the Foil Temperature using OES

Figure 2(a) shows emission spectra from the plasma with and without Cu foil. The emission spectrum without the inclusion of foil exhibits only narrow spectral lines originating from active plasma species (such as Ar, Ar$^+$, H$_2$ and H) [11, 14]. The plasma emission with the presence of Cu foil has similar narrow spectral lines, but with a broad baseline that represents blackbody emission from the Cu substrate. Thus, the temperature of the foil can be determined from its emission (using Eq. 1) which was measured at different vertical positions along the foil to validate the heat transfer model at various web speeds for Ni and Cu foils.

Figures 2(b) and 2(c) show the emission spectra of Cu and Ni foils, respectively. At a web speed of 0 mm/min, the Cu (Ni) foil temperature decreases slightly from its peak of 1100 K (985 K) at the plasma centerline, around $y = 0.49$ m, to 1045 K (962 K) at the plasma edge, around $y = 0.46$ m (as indicated in Fig. 1(c)). This temperature drop occurs because of heat loss by conduction to the lower temperature pre-plasma region. In addition, the temperature at the plasma edge, around $y = 0.46$ m, reduces further to 960 K and 938 K for Cu and Ni, respectively, when the foil is moving downward at a web speed of 50 mm/min. Advection of the moving foil lowers the substrate temperature, especially near the plasma edge.

4.2 Temperature Distributions on Cu and Ni Foils during the Roll-to-roll Process

Figure 3 presents the temperature distributions of Cu and Ni foils based on experiment and model at web speeds of 0, 50 and 150 mm/min. The temperature of both Ni and Cu foils is high in the plasma region due to the elevated gas temperature in the plasma $T_{\infty 2}$. Due to the lower thermal conductivity of Ni (72 W/m.K at 1000 K [33]), its temperature at 0 mm/min remains more uniform in the plasma region in comparison to the Cu foil, which exhibits a strong decaying profile because of its higher thermal conductivity (352 W/m.K at 1000 K [33]). Consequently, Ni foil conducts less heat to the pre- and post-plasma regions, and the substrate temperature reaches the gas temperatures $T_{\infty 1}$ and $T_{\infty 3}$ more readily. For Cu, because of its higher thermal conductivity, the temperature field penetrates to longer distances in the pre- and post-plasma regions.

At the given web speeds, Ni foil has a lower peak temperature in the plasma region than Cu foil. This temperature difference is related to the higher emissivity of Ni, which is 0.14, compared to 0.04 for Cu at 1000 K [33]. Hence, Ni foil
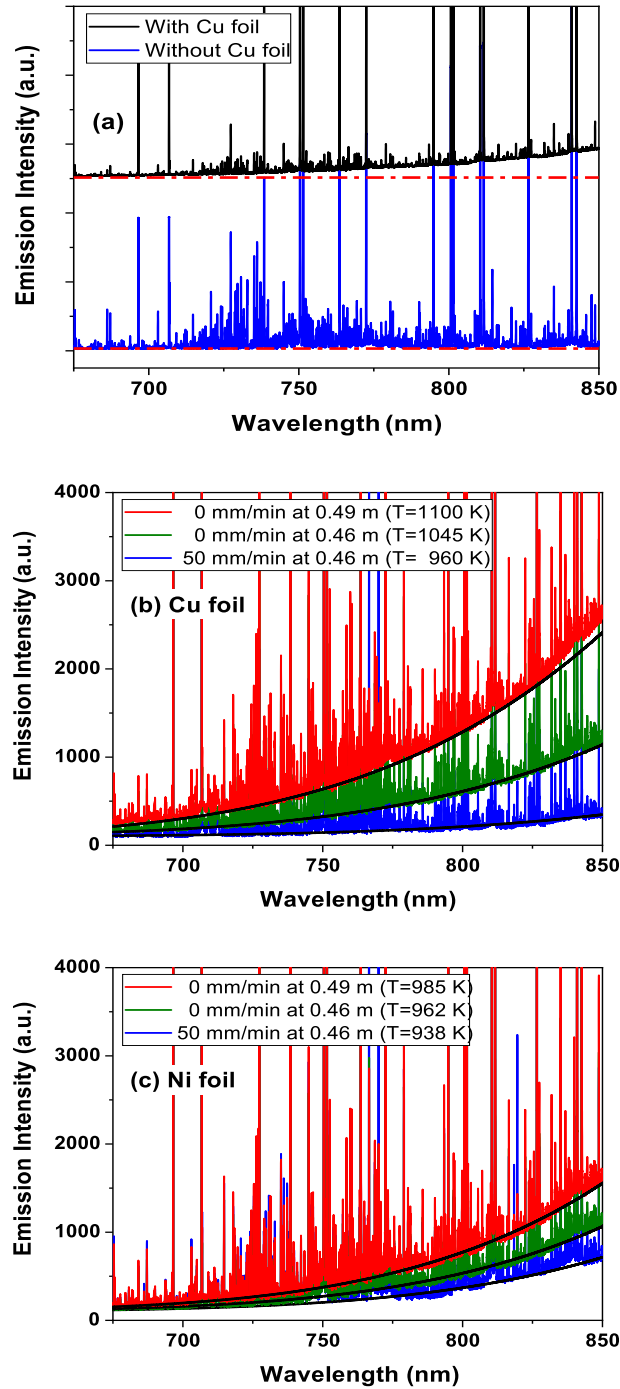
Fig. 2: (a) Emission spectra from the plasma with and without the Cu foil, showing the broad baseline with the inclusion of foil. The variation of substrate emission for (b) Cu and (c) Ni as a function of position and web speed in the plasma region. The substrate temperature is included in legends of (b) and (c) and is derived from the corresponding Planck's distribution fitting (Eq. 1).

experiences higher radiation exchange with the low-temperature chamber wall and plasma electrodes, resulting in a higher heat loss from Ni foil than from Cu foil in the plasma region [38].

As illustrated in Fig. 3, both Ni and Cu foil temperature profiles evolve as a result of heat advection via foil movement. As web speed increases from 0 to 150 mm/min, the temperature profile becomes asymmetric with lower and higher temperatures in the pre- and post-plasma regions, respectively. The peak temperature in the plasma region decreases with increased web speed due to the cooling effect provided by advection of the moving foil. Furthermore, the position of peak temperature

shifts downstream as web speed increases. Hence, the temperature of the foil has less uniformity in the plasma region with increased web speed.

Moreover, the temperatures in the pre-plasma region decrease with increased web speed due to the higher value of the exponent in the temperature distribution of Eq. 6 (i.e., $(\sqrt{a^2 + 4m_1} + a)$, where $a = \frac{\rho U c_P}{k}$ and U is the web speed). Thus, as web speed increases, more heat is carried downward by the moving foil. On the other hand, the exponent in the temperature distribution for the post-plasma region of Eq. 6 (i.e., $(\sqrt{a^2 + 4m_3} - a)$) decreases with increased web speed, resulting in a higher substrate temperature. In other words, the foil needs a longer distance to cool to the ambient gas temperature ($T_{\infty 3}$) as web speed increases [31, 38, 39].

Furthermore, Ni has a higher advective Pe number than Cu because of the former's low thermal diffusivity, resulting in larger heat transfer by advection than diffusion processes in Ni foil [33]. The advective Pe number is defined as $Pe = \frac{LU}{\alpha}$, where α is the thermal diffusivity of the foil, L is the plasma length, and U is the web speed. For example, Pe number for Ni increases from 7.3 at 50 mm/min to 21.8 at 150 mm/min, whereas Pe number rises slightly from 1.2 to 3.6 for Cu for the same web speeds. Hence, the temperature distribution of Ni foil changes more considerably than Cu foil with web speed.

The temperature distribution from the model is fitted with experimental measurements to find the best fit of h_2 at various web speeds for Cu and Ni foils as shown in the inset of Fig. 3. The best-fit values of h_2 are 55, 30, and 29 W/m^{2}K for Cu, and 36, 30, and 28 W/m^{2}K for Ni at 0, 50, and 150 mm/min, respectively. The difference in h_2 between Cu and Ni is low with increased web speed indicating lessened interactions of the plasma gas with the foil. However, h_2 is higher for Cu than Ni at 0 mm/min which could be related to the difference in their temperatures with the plasma gas temperature. The fluid flow characteristics adjacent to the foil, which have not been assessed in this work because of their complexity, could be altered leading to the difference in h_2 for Cu and Ni at 0 mm/min. The uncertainty bands on h_2 are derived by finding the best fit of the model to the minimum and maximum values of the foil temperature measurements which are 990 and 1210 K, respectively (which is 10% of the plasma gas temperature, 1100 K). For example, the range of h_2 for Cu foil are 29-80 W/m^{2}K at 0 mm/min, 17-60 W/m^{2}K at 50 mm/min and 17-50 W/m^{2}K at 150 mm/min. Similarly, the range of h_2 for Ni foil are 20-65 W/m^{2}K at 0 mm/min, 17-55 W/m^{2}K at 50 mm/min and 17-50 W/m^{2}K at 150 mm/min.

Furthermore, a sensitivity analysis is made to determine the influence of the main input parameters (including h_2) on the model as shown in Table S-2, and Figs. S-7 and S-8 in the Supporting Information. The model is more sensitive to change in the plasma gas temperature ($T_{\infty 2}$), followed by the electrode temperatures (T_{RE} and T_{LE} for the right and left electrodes, respectively), the heat transfer coefficient in the plasma region (h_2) and the foil emissivity (ε). The gas temperature in the pre-plasma region ($T_{\infty 1}$), heat transfer coefficient in the pre-plasma region (h_1), and velocity (U) have negligible sensitivity coefficients on model. Also, $T_{\infty 2}$, h_2, T_{RE} and T_{LE} have positive sensitivity coefficients, whereas ε has a negative sensitivity coefficient that indicates a reduced foil temperature with increased emissivity.

4.3   Roll-to-Roll Deposition of Graphene on Ni and Cu Foils

Graphene can be deposited on Ni foil during the R2R process with different qualities and thicknesses, depending on the web speed. Figure 4 shows SEM images of deposited films on Ni with substantial differences in contrast and morphology for different web speeds. The graphene thickness varies significantly across the Ni surface at 0 mm/min, as shown in Figs. 4(a) and 4(b). The darker regions represent thicker carbon films, whereas the lighter regions suggest the presence of graphene with a reduced number of layers. This thickness variation within the sample likely arises from the various orientations in the polycrystalline Ni foil that have distinct carbon precipitation rates during the substrate cooling period [40–42].

Conversely, as web speed increases, the uniformity of graphene is considerably enhanced, as shown in the SEM images of Figs. 4(c) and 4(e), with web speeds of 50 and 150 mm/min, respectively. Furthermore, the contrast between the images in Figs. 4(d) and 4(f) decreases with higher web speed (or lower residence time), indicating decreased graphene thickness. With increased residence time in the plasma, the thickness increases because of the larger concentration of dissolved carbon atoms in Ni [43].

Raman spectra of graphene on Ni foil are shown in Fig. 5 as a function of web speed. Raman peaks of graphene include the D peak at 1350 cm^{-1}, G peak at 1580 cm^{-1}, D′ peak at 1620 cm^{-1} and 2D peak at 2700 cm^{-1} [44,45]. The D and D′ peaks occur because of defects in the graphene lattice, whereas the G and 2D peaks are signatures of graphitic films. The intensity ratio of the 2D and G peaks (I_{2D}/I_G) at 0 mm/min is 0.31. However, as web speed increases to 50 and 150 mm/min, the I_{2D}/I_G ratio drops to 0.20 and 0.12, respectively. The 2D peak decreases with increased web speed because of the decreased foil residence time in the plasma and the lower substrate temperature that minimizes carbon diffusion [42].

The I_D/I_G peak ratio, which represents relative defect density, suggests that the deposited graphene is negatively affected by ion bombardment from plasma species such as Ar$^+$ [11]. The I_D/I_G ratio values on Ni remain similar at around 1.4 as a function of web speed. The D′ peak is present at 0 mm/min, whereas this peak disappears as web speed increases (Fig. 5). In addition, the G peak position shifts from 1586 cm^{-1} at 0 mm/min to 1602 cm^{-1} at 50 mm/min and finally to 1606 cm^{-1} at 150 mm/min. The roll-to-roll process could induce strain in the carbon films that results in the shift of G-peak position from its original position of 1580 cm^{-1} to 1586 cm^{-1} at 0 mm/min [10]. However, the shift of the G-peak and the disappearance of the D′ peak with increased web speed could be related to the existence of higher strain and larger disorder in the graphene
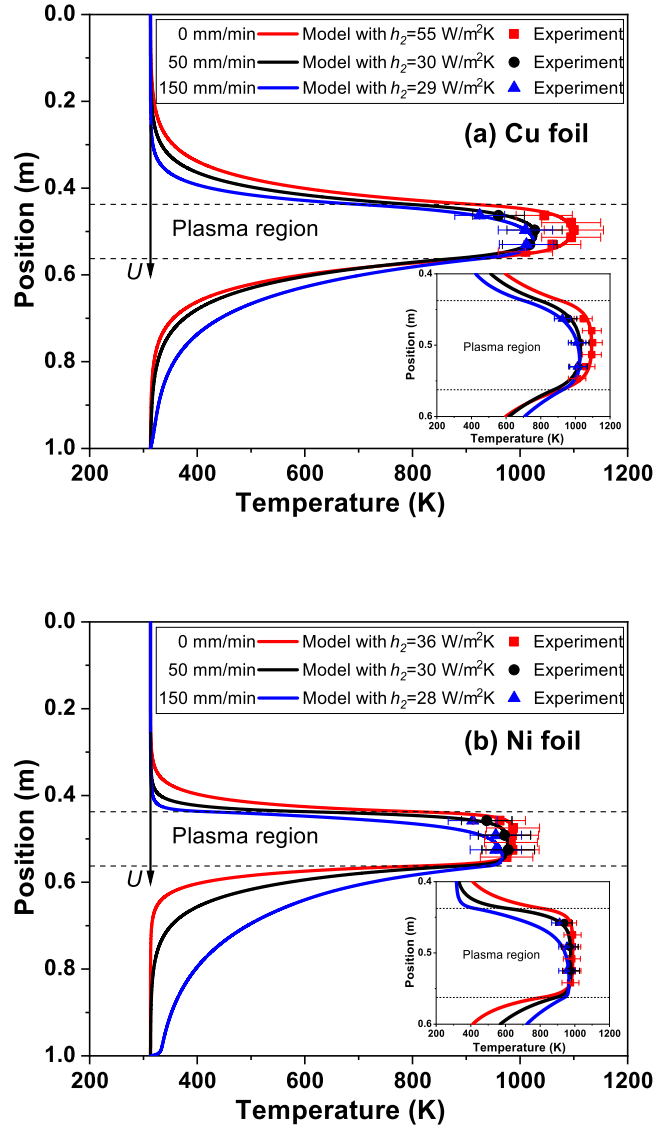
Fig. 3: Effects of web speed on the temperature distributions of (a) Cu foil and (b) Ni foil based on experiment and model. The best fit of h_2 (the convective heat transfer coefficient in the plasma region) is included for each temperature distribution from the model. The sensitivity of the model to h_2 and other input parameters are discussed in the main text. The insets in (a) and (b) present the local temperature distributions near the plasma region.

lattice, leading to the broadening of the G-peak and its possible overlap with D$'$-peak [46, 47].

Graphene deposition on Cu foil exhibits better uniformity than on Ni foil but with a lower thickness of deposited film as web speed increases, as also reported in our previous work [11]. However, the quality of graphene on Cu foil varies significantly with web speed [7, 11, 14]. Table 1 compares results from Raman spectroscopy of graphene on Ni and Cu foils as a function of web speed. Unlike graphene on Ni foil, the I_D/I_G ratio of graphene on Cu foil decreases steeply with increased web speed. For example, the I_D/I_G ratio of graphene on Cu is higher than graphene on Ni at 0 mm/min. However, the I_D/I_G ratio on Cu drops significantly to 0.76 and 0.66 with increased web speeds of 50 and 150 mm/min, respectively. This decline of the I_D/I_G ratio of graphene on Cu with web speed is opposite to previous results using a thermal CVD system [7]. Decreasing the residence time in the plasma minimizes the defects created by ion bombardment, because graphene growth on Cu occurs during its exposure to the plasma where ample supply of intermediate carbon species exists to accelerate graphene growth on Cu by catalytic reactions on its surface [48]. On the other hand, the I_D/I_G ratio of graphene on Ni varies little with the reduction of residence time since the growth process is primarily driven by carbon diffusion and the segregation/precipitation process in the post-plasma region.
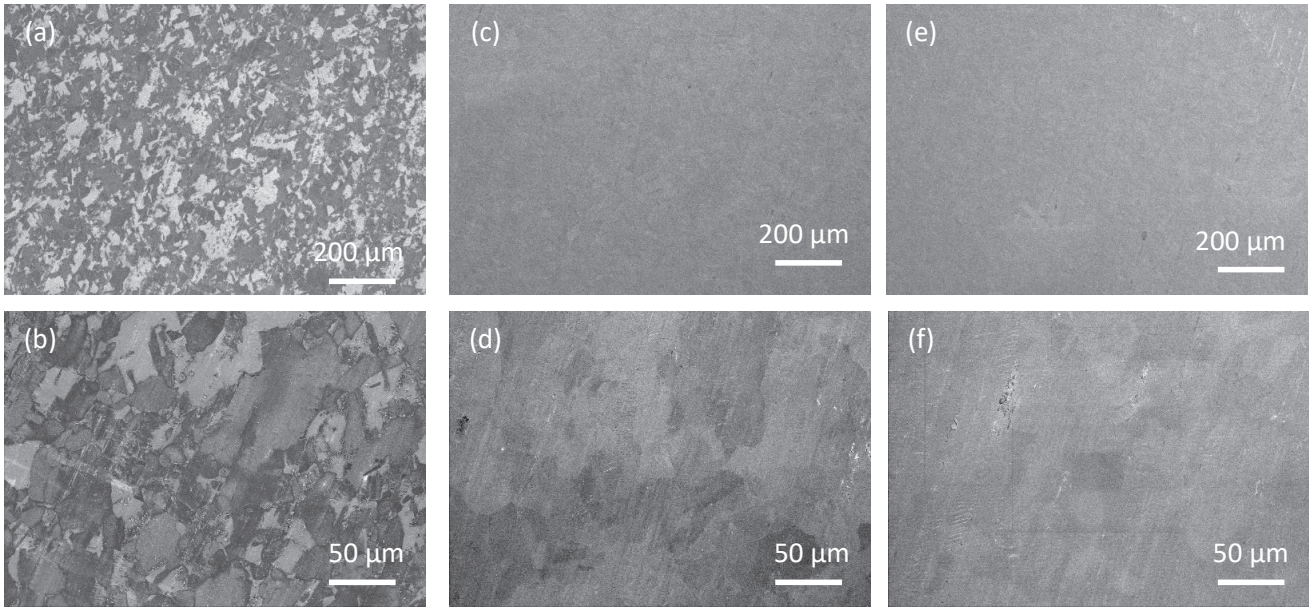
Fig. 4: SEM images of graphene on Ni foil at web speeds of (a) and (b) 0 mm/min; (c) and (d) 50 mm/min; and (e) and (f) 150 mm/min
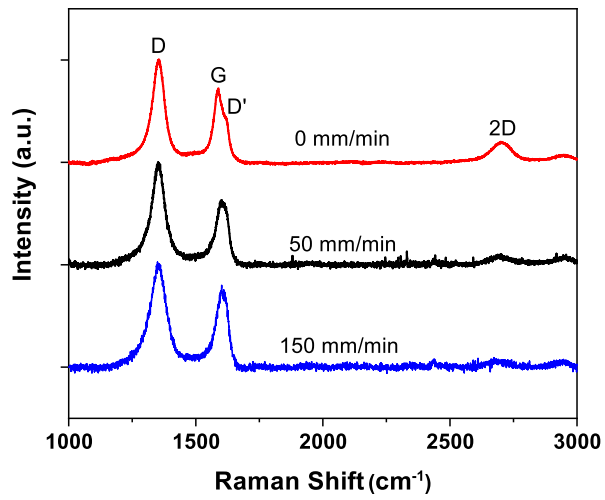

Fig. 5: Raman spectra of graphene on Ni foil as a function of web speed

Table 1: Comparison between the intensity ratios of Raman peaks for graphene on Ni and Cu foils at various web speeds

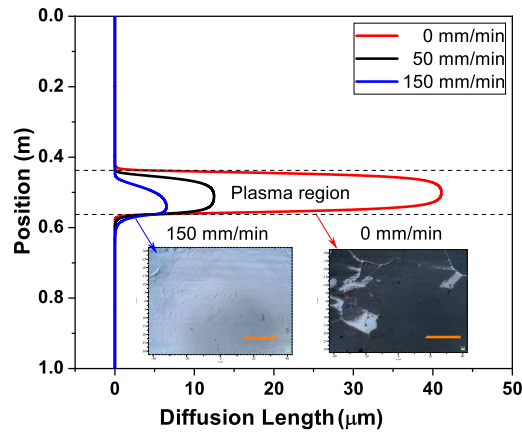| Web Speed (mm/min)	I_D/I_G (Ni foil)	I_{2D}/I_G (Ni foil)	I_D/I_G (Cu foil)	I_{2D}/I_G (Cu foil)
0	1.37	0.31	1.61	0.53
50	1.56	0.20	0.76	0.10
150	1.25	0.12	0.66	0.07

Fig. 6: Diffusion length of carbon atoms in Ni foil at various web speeds. Optical images of graphene on Ni foil at 0 and 150 mm/min are included to demonstrate the deposition of a thick graphite film at 0 mm/min in contrast to uniform growth of few-layer graphene at 150 mm/min. The scale bar in the optical images is 20 μm.

Furthermore, the I_{2D}/I_G ratio for graphene on Cu declines sharply from 0.53 at 0 mm/min to 0.10 at 50 mm/min (Table 1). The 2D peak is negligible when the web speed is raised to 150 mm/min. The I_{2D}/I_G ratio is larger for Cu than Ni at the null speed, but the I_{2D}/I_G ratio of graphene on Cu becomes lower than on Ni at 50 and 150 mm/min. The variation of the I_{2D}/I_G ratio with web speed found here is similar to previous results in a R2R thermal CVD system [7]. Decreased residence time of Cu foil in the plasma region with increased web speed could affect growth kinetics, especially for lower Cu foil temperatures at which the graphene growth rate is very low [49]. Thus, the graphitization processes are hindered at lower substrate temperatures and shorter residence times because of less active C atoms at the Cu surface.

Indeed, the changes of the temperature distributions of Ni and Cu foils with web speed strongly affects the quality of graphene growth in a R2R process. Increasing the web speed to 150 mm/min minimizes the foil temperature in the pre-plasma region and lowers the temperature uniformity in the plasma region in which graphene growth occurs. These temperature changes, combined with reduced residence time with increased web speed, affect the growth kinetics of graphene by altering catalytic reactions of methane on Cu foil, carbon diffusion in Ni foil, and the heating and cooling rates of the Cu and Ni foils as discussed below.

4.4 Correlations between Graphene Growth and Temperature Distribution of Ni and Cu Foils

The variations of graphene thickness and uniformity on Ni foil with web speed in Fig. 4 can be clarified first by estimating the diffusion length of carbon atoms in the Ni substrate during the growth process. The diffusion length (L_D) is defined as: $L_D = 2\sqrt{D_T t}$ where t is the Ni foil residence time in the plasma region: 1278, 150, and 50 seconds at 0, 50, and 150 mm/min web speeds, respectively. Carbon diffusivity, D_T, depends on Ni foil temperature, T, as: $D_T = D_o exp\left(-\frac{E_D}{k_B T}\right)$ where k_B is Boltzmann's constant which is 8.617x10^{-5} eV/K [21, 50, 51]. Also, D_o equals 2.4818 cm^2/s and E_D equals 1.74 eV representing the entropic pre-factor and the diffusion activation energy, respectively [21, 52].

Figure 6 illustrates the diffusion length of carbon in Ni as a function of web speed. At 0 mm/min, the diffusion length is about 41.1 μm, which is slightly greater than half of the Ni foil thickness which is 38.1 μm. Hence, carbon atoms can diffuse throughout the Ni foil since its both sides are exposed to plasma. Diffused carbon atoms are expected to precipitate and segregate on the Ni surface during the cooling stage, yielding a thick carbon film as seen in the corresponding optical image at 0 mm/min in Fig. 6 and the SEM images of Figs. 4(a) and 4(b).

Because of the decline in both the residence time and substrate temperature with increased web speed, the diffusion length drops to 12.5 and 6.5 μm at 50 and 150 mm/min, respectively. Therefore, less carbon can dissolve into the Ni foil as web speed increases, leading to the growth of graphene with lower thickness as evident from the SEM images at 150 mm/min (Figs. 4(e) and 4(f)) and the optical image of graphene on Ni at 150 mm/min (Fig. 6). On the other hand, because carbon solubility is negligible in Cu, the growth of graphene on Cu is controlled not by diffusion processes as in Ni, but rather by catalytic reactions of carbon species on Cu at high temperatures [13].

In addition, the rate of temperature change ($\frac{dT}{dt}$) is derived by taking the first derivative of the temperature distribution ($\frac{dT}{dy}$) and applying the chain rule: $\frac{dT}{dt} = \frac{dT}{dy}\frac{dy}{dt} = U\frac{dT}{dy}$, where U is the web speed. Here, the derivative of the temperature distribution from the numerical model (Eq. 8) is used to find the rate of temperature change as a function of position ($\frac{dT}{dy}$). The heating and cooling rates of the foil occur in the pre- and post-plasma regions, respectively.

Figure 7 presents the heating and cooling rates of Cu and Ni foils at 50 and 150 mm/min. The heating rate of the foil is higher than the cooling rate of the foil. Both rates are non-linear because of variations in the foil temperature in the three regions due to convection, radiation and advection processes. Also, Ni has higher heating and cooling rates than Cu, which exhibits more gradual changes. These differences arise from the distinct temperature distributions of Ni and Cu, primarily due to the high thermal conductivity of the latter (Fig. 3).
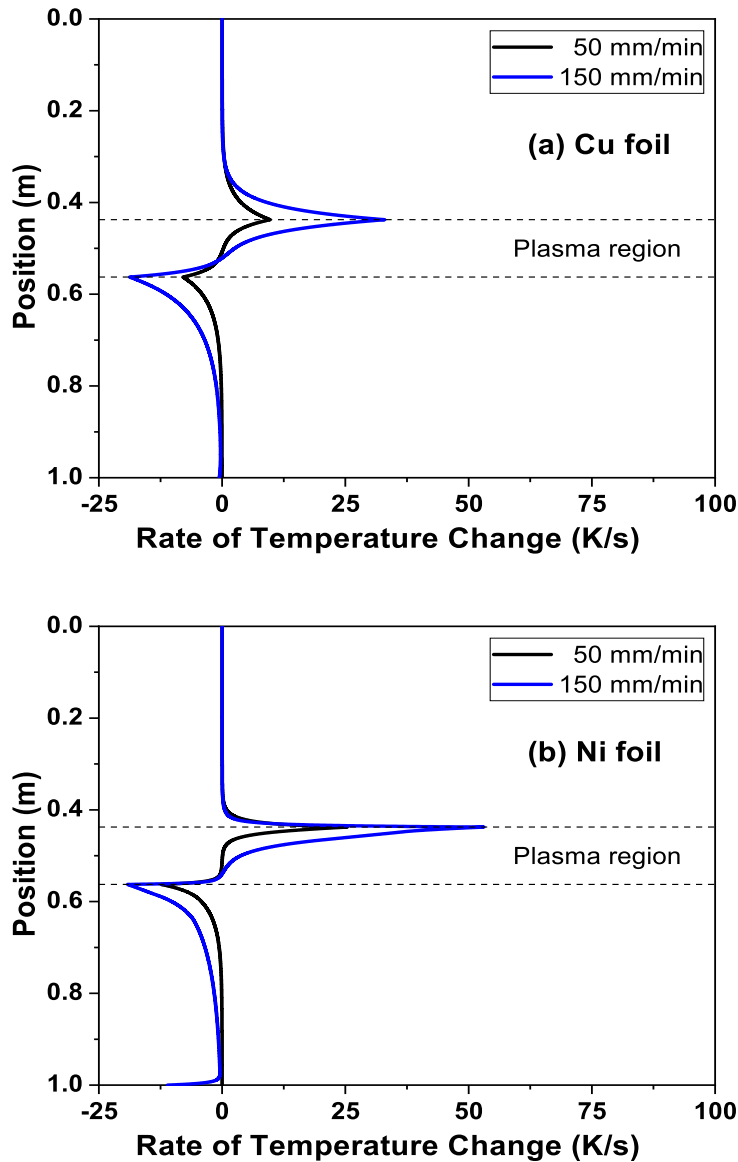

Fig. 7: The rate of temperature change for (a) Cu and (b) Ni foils during the R2R process at 50 and 150 mm/min

Web speed significantly influences both the heating and cooling rates because of the substantial contribution from the advection term to the temperature distribution profiles (Fig. 3). For instance, at the interface of the pre-plasma and plasma regions, the heating rate increases sharply since the foil enters the plasma region rapidly. Similarly, the maximum cooling rates in the post-plasma region rise with increased web speed, with values of 12.3 and 19.2 K/s at 50 mm/min and 150 mm/min, respectively, for Ni foil. On the other hand, Cu has lower maximum cooling rates of 7.9 and 18.7 K/s at 50 and 150 mm/min, respectively.

The cooling rate decreases exponentially as the foil moves to the bottom spool until the substrate temperature equilibrates with the temperature of the spool (i.e., the gas temperature in the post-plasma region, $(T_{\infty 3})$). However, at 150 mm/min, the foil requires a longer distance to cool to the post-plasma gas temperature, which explains the sharp rise in the cooling rate

near the bottom spool, as shown in Fig 7.

Consequently, uniform deposition of few-layer graphene on Ni foil can be achieved at high web speeds of 50 and 150 mm/min. However, due to the decreased Cu foil temperature with increased web speed (Fig. 3), the catalytic reactions of CH_4 (and other carbon species) limit the production rate of high-quality graphene on Cu [53]. For example, the I_{2D}/I_G ratio for graphene on Cu is negligible at 50 and 150 mm/min as presented in Table 1. Hence, the improved I_{2D}/I_G ratio for graphene on Ni is likely due to diffusion/segregation processes that drive the growth on Ni rather than by surface catalysis reactions, which are strongly temperature-dependent. Furthermore, because of the lower diffusion length and higher cooling rate with increased web speed, graphene uniformity on Ni foil is improved at higher web speeds, allowing for higher throughput of graphene deposition than would be possible on Cu foil.

4.5 Influence of Ni Foil Thickness on Temperature Distribution and Cooling Rate

The difference of cooling rates associated with the successful growth of few-layer graphene on Ni listed in Table S-1 can be correlated with substrate thickness as demonstrated in Fig. 8(a). A lower cooling rate (less than 1 K/s) yields graphene films on Ni substrate with thicknesses of less than 10 μm. However, the successful deposition of graphene on thicker Ni (greater than 10 μm) is reported at cooling rates higher than 1 K/s.

The model is used to understand the effects of Ni thickness on the temperature distribution and cooling rate at three thickness values of Ni: 5, 50 and 500 μm in accordance with the previous reports. The other input parameters are the same as in Fig. 3(b) for Ni foil at 50 mm/min. Heat transfer by advection and conduction within the foil is enhanced with increasing thickness (through increasing the cross-sectional area), leading to a higher temperature in the post-plasma region with increased thickness (Fig. 8(b)). The foil requires a longer distance to cool to $T_{\infty 3}$ for the 500 μm-thick Ni foil, whereas the 5 μm-thick foil equilibrates thermally with the ambient gas in the pre-plasma region ($T_{\infty 3}$) over a short distance (less than 20 cm after leaving the plasma region).

The cooling rate at various thicknesses is shown in Fig. 8(c). The 5 μm-thick foil cools quickly with a maximum rate of 59.9 K/s at 0.56 m, which then decreases sharply with position until it becomes 0.1 K/s at 0.65 m. Therefore, the reported low cooling rates for thin Ni substrates in Fig. 8(a) could be due to the fact that the substrate temperature decreases sharply after the growth period, as illustrated in Fig. 8(c) for 5 μm-thick foil. The additional slow cooling rate of less than 0.1 K/s for the 5 μm-thick foil is not expected to contribute to graphene synthesis since the initial fast cooling rate can impede carbon from diffusing from the Ni surface to the bulk gas (Fig. 8(c)). Hence, the additional slow cooling rate, which lasts for a longer distance (a surrogate of time in Fig. 8(c)), can minimize the averaged cooling rate of the 5 μm-thick Ni foil.

On the other hand, the cooling rate for the substrate at 500-μm is initially lower than the substrates at 5 and 50 μm. The maximum cooling rate for the 500-μm foil is 2.7 K/s at 0.56 m, gradually decreasing to 0.4 K/s at 0.93 m. The cooling rate becomes higher for the 500 μm foil than the other foils starting at cross-over positions of 0.60 and 0.64 m for 5 and 50 μm foils, respectively, as shown in the inset of Fig. 8(c). On average, thicker Ni substrates are cooled at a faster rate to allow graphene growth to avoid the diffusion of carbon back to the bulk gas [15, 43]. For instance, graphene sheets were not observed when the cooling rate was 0.1 K/s for Ni substrate of 500 μm thickness [15], whereas graphene films were detected in the same cooling rate range using thinner Ni substrates as summarized in Fig. 8(a). Nevertheless, graphene can be deposited on thin Ni substrates using a higher cooling rate of 10 K/s [17].

The effects of other process conditions such as the gas mixture (particularly the carbon source and its concentration), growth temperature, gas pressure, and growth time play important roles in graphene deposition [16, 18, 20, 40, 43, 54–58]. These parameters affect the solubility of carbon atoms upon methane (or another carbon source) addition for graphene deposition. For instance, Reina et al. reported the influence of methane concentration on graphene deposition with Ni substrates at various cooling rates [16]. They found that graphene was deposited using methane fractions of 0.5 vol% and 0.6 vol%, whereas a lower methane concentration of 0.4 vol% did not yield graphene even though the same cooling rate and substrate thickness was used for these experiments [16]. Hence, these parameters should be optimized to control the amount of carbon dissolved in Ni to allow successful graphene deposition.

5 Conclusions

Temperature distributions of Ni and Cu foils during roll-to-roll deposition of graphene have been determined through a combined experimental, analytical, and numerical study. The maximum substrate temperature, which occurs in the high-temperature plasma region, decreases with increasing web speed caused by higher heat advection of the moving foil. Consequently, graphene deposition on Cu foil declines with increased web speed since the growth mechanism is catalytically driven with less contribution from carbon diffusion. The throughput of graphene production can be increased by utilizing Ni as a substrate because carbon solubility in Ni is higher than in Cu. Accordingly, carbon films can be deposited on Ni foil within a variety of thicknesses, from few-layer graphene to thin graphite films, depending on web speed.

The cooling rate of the substrate during the R2R process is derived from basic heat transfer principles, correlating the cooling rate with web speed. Thus, due to high carbon solubility in Ni, graphene can be deposited at higher web speeds
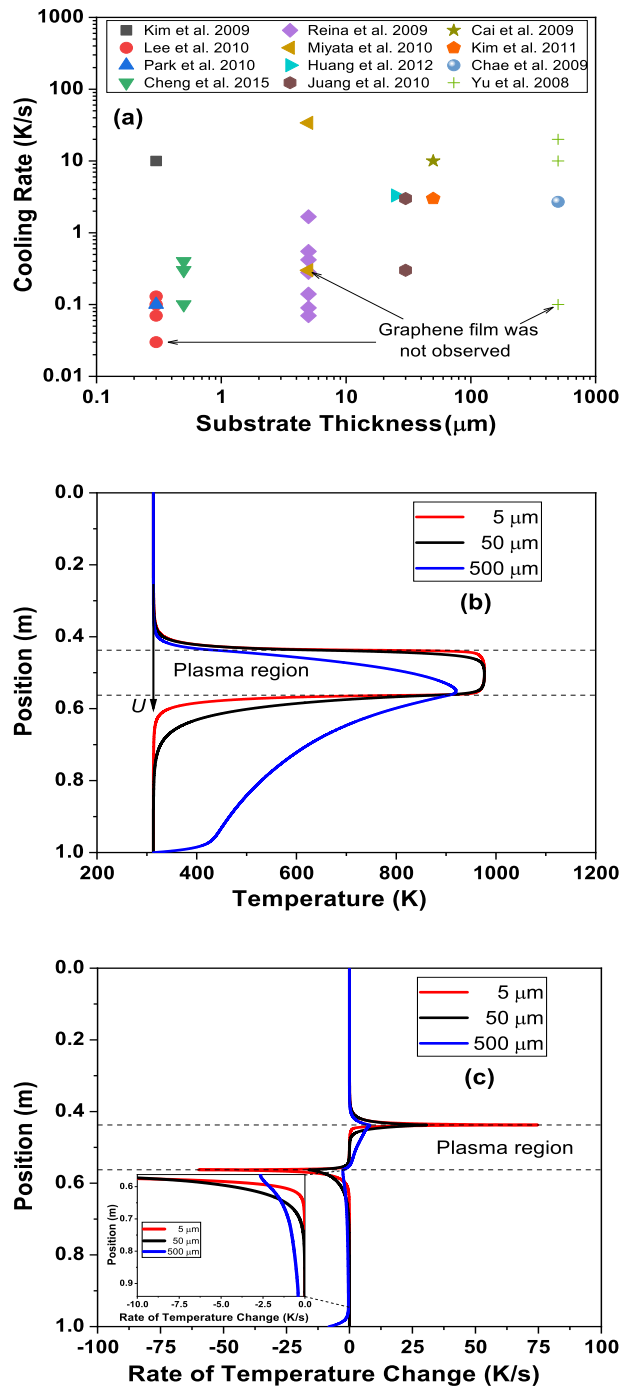
Copyright © by ASME

Fig. 8: Effects of Ni substrate thickness on: (a) the cooling rate from previous studies, (b) the temperature distribution from the model, and (c) the rate of temperature change from the model. The web speed is fixed at 50 mm/min in (b) and (c), and the other input parameters are similar to the case at 50 mm/min in Fig. 3(b).

because of enhanced cooling rates. Thin Ni foils offered higher temperature with better uniformity and faster cooling rate, allowing for controlled deposition of few-layer graphene films. These findings reveal the importance of using heat transfer analysis to optimize graphene deposition on Ni and other substrates with high carbon solubility in a R2R process. Even though uniform graphene was successfully deposited on Ni at high web speed, the temperature distribution, which strongly depends on web speed, affects the quality of the deposited graphene. Hence, to further improve the throughput deposition of graphene on Ni or Cu, separate temperature-controlled pre- and post-growth regions could be utilized to regulate heating and cooling rates independently.

Supporting Information

Supporting information is available online from ASME Online Library or from the corresponding author.

References

[1] Novoselov, K. S., Jiang, D., Schedin, F., Booth, T., Khotkevich, V., Morozov, S., and Geim, A. K., 2005. "Two-dimensional atomic crystals". *Proceedings of the National Academy of Sciences,* **102**(30), pp. 10451–10453.

[2] Novoselov, K. S., Geim, A. K., Morozov, S. V., Jiang, D., Katsnelson, M. I., Grigorieva, I., Dubonos, S., and Firsov, A., 2005. "Two-dimensional gas of massless dirac fermions in graphene". *Nature,* **438**(7065), pp. 197–200.

[3] Geim, A. K., and Novoselov, K. S., 2007. "The rise of graphene". *Nature Materials,* **6**, p. 183–191.

[4] Novoselov, K. S., Fal, V., Colombo, L., Gellert, P., Schwab, M., Kim, K., et al., 2012. "A roadmap for graphene". *Nature,* **490**(7419), pp. 192–200.

[5] Bae, S., Kim, H., Lee, Y., Xu, X., Park, J.-S., Zheng, Y., Balakrishnan, J., Lei, T., Kim, H. R., Song, Y. I., et al., 2010. "Roll-to-roll production of 30-inch graphene films for transparent electrodes". *Nature Nanotechnology,* **5**(8), p. 574.

[6] Hesjedal, T., 2011. "Continuous roll-to-roll growth of graphene films by chemical vapor deposition". *Applied Physics Letters,* **98**(13), p. 133106.

[7] Polsen, E. S., McNerny, D. Q., Viswanath, B., Pattinson, S. W., and Hart, A. J., 2015. "High-speed roll-to-roll manufacturing of graphene using a concentric tube cvd reactor". *Scientific Reports,* **5**(1), pp. 1–12.

[8] Zhong, G., Wu, X., D'Arsie, L., Teo, K. B., Rupesinghe, N. L., Jouvray, A., and Robertson, J., 2016. "Growth of continuous graphene by open roll-to-roll chemical vapor deposition". *Applied Physics Letters,* **109**(19), p. 193103.

[9] Kobayashi, T., Bando, M., Kimura, N., Shimizu, K., Kadono, K., Umezu, N., Miyahara, K., Hayazaki, S., Nagai, S., Mizuguchi, Y., et al., 2013. "Production of a 100-m-long high-quality graphene transparent conductive film by roll-to-roll chemical vapor deposition and transfer process". *Applied Physics Letters,* **102**(2), p. 023112.

[10] Yamada, T., Ishihara, M., Kim, J., Hasegawa, M., and Iijima, S., 2012. "A roll-to-roll microwave plasma chemical vapor deposition process for the production of 294 mm width graphene films at low temperature". *Carbon,* **50**(7), pp. 2615–2619.

[11] Alrefae, M. A., Kumar, A., Pandita, P., Candadai, A., Bilionis, I., and Fisher, T. S., 2017. "Process optimization of graphene growth in a roll-to-roll plasma cvd system". *AIP Advances,* **7**(11), p. 115102.

[12] Li, X., Cai, W., An, J., Kim, S., Nah, J., Yang, D., Piner, R., Velamakanni, A., Jung, I., Tutuc, E., et al., 2009. "Large-area synthesis of high-quality and uniform graphene films on copper foils". *Science,* **324**(5932), pp. 1312–1314.

[13] Mattevi, C., Kim, H., and Chhowalla, M., 2011. "A review of chemical vapour deposition of graphene on copper". *Journal of Materials Chemistry,* **21**(10), pp. 3324–3334.

[14] Alrefae, M. A., and Fisher, T. S., 2018. "Thermal analysis and optimization of graphene deposition in a roll-to-roll plasma cvd process". In International Heat Transfer Conference Digital Library, Begel House Inc., pp. 5661–5668.

[15] Yu, Q., Lian, J., Siriponglert, S., Li, H., Chen, Y. P., and Pei, S.-S., 2008. "Graphene segregated on ni surfaces and transferred to insulators". *Applied Physics Letters,* **93**(11), p. 113103.

[16] Reina, A., Jia, X., Ho, J., Nezich, D., Son, H., Bulovic, V., Dresselhaus, M. S., and Kong, J., 2009. "Large area, few-layer graphene films on arbitrary substrates by chemical vapor deposition". *Nano Letters,* **9**(1), pp. 30–35.

[17] Kim, K. S., Zhao, Y., Jang, H., Lee, S. Y., Kim, J. M., Kim, K. S., Ahn, J.-H., Kim, P., Choi, J.-Y., and Hong, B. H., 2009. "Large-scale pattern growth of graphene films for stretchable transparent electrodes". *Nature,* **457**(7230), pp. 706–710.

[18] Kim, Y., Song, W., Lee, S., Jeon, C., Jung, W., Kim, M., and Park, C.-Y., 2011. "Low-temperature synthesis of graphene on nickel foil by microwave plasma chemical vapor deposition". *Applied Physics Letters,* **98**(26), p. 263106.

[19] Obraztsov, A., Obraztsova, E., Tyurnina, A., and Zolotukhin, A., 2007. "Chemical vapor deposition of thin graphite films of nanometer thickness". *Carbon,* **45**(10), pp. 2017–2021.

[20] Cheng, L., Yun, K., Lucero, A., Huang, J., Meng, X., Lian, G., Nam, H.-S., Wallace, R. M., Kim, M., Venugopal, A., et al., 2015. "Low temperature synthesis of graphite on ni films using inductively coupled plasma enhanced cvd". *Journal of Materials Chemistry C,* **3**(20), pp. 5192–5198.

[21] Lander, J., Kern, H., and Beach, A., 1952. "Solubility and diffusion coefficient of carbon in nickel: reaction rates of nickel-carbon alloys with barium oxide". *Journal of Applied Physics,* **23**(12), pp. 1305–1309.

[22] Sakiadis, B. C., 1961. "Boundary-layer behavior on continuous solid surfaces: I. boundary-layer equations for two-dimensional and axisymmetric flow". *AIChE Journal,* **7**(1), pp. 26–28.

[23] Tsou, F., Sparrow, E. M., and Goldstein, R. J., 1967. "Flow and heat transfer in the boundary layer on a continuous moving surface". *International Journal of Heat and Mass Transfer,* **10**(2), pp. 219–235.

[24] Lee, S., and Tsai, J., 1990. "Cooling of a continuous moving sheet of finite thickness in the presence of natural convection". *International Journal of Heat and Mass Transfer,* **33**(3), pp. 457–464.

[25] Karwe, M., and Jaluria, Y., 1986. "Thermal transport from a heated moving surface". *JOURNAL OF HEAT TRANSFER-TRANSACTIONS OF THE ASME,* **108**(4), pp. 728–733.

[26] Char, M.-I., Cha, O., Chen, K., and Cleaver, J. W., 1990. "Conjugate forced convection heat transfer from a continuous, moving flat sheet". *International Journal of Heat and Fluid Flow,* **11**(3), pp. 257–261.

[27] Comini, G., Savino, S., Magriotis, N., and Muratori, S., 2007. "Thermal modeling of vacuum web coating". *Applied thermal engineering,* **27**(2-3), pp. 611–618.

[28] Cobos Torres, E. O., and Pagilla, P. R., 2017. "Temperature distribution in moving webs heated by radiation panels: model development and experimental validation". *Journal of Dynamic Systems, Measurement, and Control,* **139**(5).

[29] Aziz, A., and Lopez, R. J., 2011. "Convection-radiation from a continuously moving, variable thermal conductivity sheet or rod undergoing thermal processing". *International Journal of Thermal Sciences,* **50**(8), pp. 1523–1531.

[30] Karwe, M., and Jaluria, Y., 1991. "Numerical simulation of thermal transport associated with a continuously moving flat sheet in materials processing". *JOURNAL OF HEAT TRANSFER-TRANSACTIONS OF THE ASME,* **113**(3), pp. 612–619.

[31] Choudhury, S. R., and Jaluria, Y., 1994. "Analytical solution for the transient temperature distribution in a moving rod or plate of finite length with surface heat transfer". *International Journal of Heat and Mass Transfer,* **37**(8), pp. 1193–1205.

[32] Saviers, K. R., Alrefae, M. A., and Fisher, T. S., 2018. "Roll-to-roll production of graphitic petals on carbon fiber tow". *Advanced Engineering Materials,* **20**(8), p. 1800004.

[33] Bergman, T. L., Incropera, F. P., DeWitt, D. P., and Lavine, A. S., 2011. *Fundamentals of heat and mass transfer.* John Wiley & Sons.

[34] Luque, J., Juchmann, W., Brinkman, E., and Jeffries, J., 1998. "Excited state density distributions of h, c, c2, and ch by spatially resolved optical emission in a diamond depositing dc-arcjet reactor". *Journal of Vacuum Science & Technology A: Vacuum, Surfaces, and Films,* **16**(2), pp. 397–408.

[35] Shivkumar, G., Tholeti, S., Alrefae, M., Fisher, T., and Alexeenko, A., 2016. "Analysis of hydrogen plasma in a microwave plasma chemical vapor deposition reactor". *Journal of Applied Physics,* **119**(11), p. 113301.

[36] Nunomura, S., Kondo, M., and Akatsuka, H., 2006. "Gas temperature and surface heating in plasma enhanced chemical-vapour-deposition". *Plasma Sources Science and Technology,* **15**(4), p. 783.

[37] Murthy, J. Y., 2002. Numerical methods in heat, mass, and momentum transfer. Draft notes, School of Mechanical Engineering, Purdue University.

[38] Karwe, M., and Jaluria, Y., 1988. "Fluid flow and mixed convection transport from a moving plate in rolling and extrusion processes". *JOURNAL OF HEAT TRANSFER-TRANSACTIONS OF THE ASME,* **110**(3), pp. 655–661.

[39] Kang, B., Yoo, J., and Jaluria, Y., 1994. "Experimental study of the convective cooling of a heated continuously moving material". *JOURNAL OF HEAT TRANSFER-TRANSACTIONS OF THE ASME,* **116**(1), pp. 199–208.

[40] Park, H. J., Meyer, J., Roth, S., and Skákalová, V., 2010. "Growth and properties of few-layer graphene prepared by chemical vapor deposition". *Carbon,* **48**(4), pp. 1088–1094.

[41] Weatherup, R. S., Bayer, B. C., Blume, R., Baehtz, C., Kidambi, P. R., Fouquet, M., Wirth, C. T., Schlögl, R., and Hofmann, S., 2012. "On the mechanisms of ni-catalysed graphene chemical vapour deposition". *ChemPhysChem,* **13**(10), pp. 2544–2549.

[42] Kozlova, J., Niilisk, A., Alles, H., and Sammelselg, V., 2015. "Discontinuity and misorientation of graphene grown on nickel foil: Effect of the substrate crystallographic orientation". *Carbon,* **94**, pp. 160–173.

[43] Chae, S. J., Güneş, F., Kim, K. K., Kim, E. S., Han, G. H., Kim, S. M., Shin, H.-J., Yoon, S.-M., Choi, J.-Y., Park, M. H., et al., 2009. "Synthesis of large-area graphene layers on poly-nickel substrate by chemical vapor deposition: wrinkle formation". *Advanced Materials,* **21**(22), pp. 2328–2333.

[44] Ferrari, A. C., and Basko, D. M., 2013. "Raman spectroscopy as a versatile tool for studying the properties of graphene". *Nature Nanotechnology,* **8**(4), pp. 235–246.

[45] Malard, L., Pimenta, M. A., Dresselhaus, G., and Dresselhaus, M., 2009. "Raman spectroscopy in graphene". *Physics Reports,* **473**(5-6), pp. 51–87.

[46] Ferrari, A. C., 2007. "Raman spectroscopy of graphene and graphite: Disorder, electron–phonon coupling, doping and nonadiabatic effects". *Solid State Communications,* **143**(1-2), pp. 47–57.

[47] Bissett, M. A., Izumida, W., Saito, R., and Ago, H., 2012. "Effect of domain boundaries on the raman spectra of mechanically strained graphene". *ACS nano,* **6**(11), pp. 10229–10238.

[48] Terasawa, T.-o., and Saiki, K., 2012. "Growth of graphene on cu by plasma enhanced chemical vapor deposition". *Carbon,* **50**(3), pp. 869–874.

[49] Kato, R., Minami, S., Koga, Y., and Hasegawa, M., 2016. "High growth rate chemical vapor deposition of graphene

under low pressure by rf plasma assistance". *Carbon,* **96**, pp. 1008–1013.

[50] Baraton, L., He, Z., Lee, C., Cojocaru, C., Châtelet, M., Maurice, J.-L., Lee, Y., and Pribat, D., 2011. "On the mechanisms of precipitation of graphene on nickel thin films". *Europhysics Letters,* **96**(4), p. 46003.

[51] Anisur, M., Banerjee, P. C., Easton, C. D., and Raman, R. S., 2018. "Controlling hydrogen environment and cooling during cvd graphene growth on nickel for improved corrosion resistance". *Carbon,* **127**, pp. 131–140.

[52] Hu, Q., Kim, S.-G., Shin, D.-W., Kim, T.-S., Nam, K.-B., Kim, M. J., Chun, H.-C., and Yoo, J.-B., 2017. "Large-scale nanometer-thickness graphite films synthesized on polycrystalline ni foils by two-stage chemical vapor deposition process". *Carbon,* **113**, pp. 309–317.

[53] Kim, H., Mattevi, C., Calvo, M. R., Oberg, J. C., Artiglia, L., Agnoli, S., Hirjibehedin, C. F., Chhowalla, M., and Saiz, E., 2012. "Activation energy paths for graphene nucleation and growth on cu". *ACS Nano,* **6**(4), pp. 3614–3623.

[54] Cai, W., Zhu, Y., Li, X., Piner, R. D., and Ruoff, R. S., 2009. "Large area few-layer graphene/graphite films as transparent thin conducting electrodes". *Applied Physics Letters,* **95**(12), p. 123115.

[55] Juang, Z.-Y., Wu, C.-Y., Lu, A.-Y., Su, C.-Y., Leou, K.-C., Chen, F.-R., and Tsai, C.-H., 2010. "Graphene synthesis by chemical vapor deposition and transfer by a roll-to-roll process". *Carbon,* **48**(11), pp. 3169–3174.

[56] Huang, L., Chang, Q., Guo, G., Liu, Y., Xie, Y., Wang, T., Ling, B., and Yang, H., 2012. "Synthesis of high-quality graphene films on nickel foils by rapid thermal chemical vapor deposition". *Carbon,* **50**(2), pp. 551–556.

[57] Miyata, Y., Kamon, K., Ohashi, K., Kitaura, R., Yoshimura, M., and Shinohara, H., 2010. "A simple alcohol-chemical vapor deposition synthesis of single-layer graphenes using flash cooling". *Applied Physics Letters,* **96**(26), p. 263105.

[58] Lee, B.-J., Yu, H.-Y., and Jeong, G.-H., 2010. "Controlled synthesis of monolayer graphene toward transparent flexible conductive film application". *Nanoscale research letters,* **5**(11), pp. 1768–1773.

A Heat Transfer Model for Graphene Deposition on Ni and Cu Foils in a Roll-to-roll Plasma Chemical Vapor Deposition System

Supporting Information

Majed A. Alrefae and Timothy S. Fisher

1   Introduction

The following table summarizes prior work involving graphene synthesis on Ni substrates.

Table S-1: Comparison of process parameters during graphene growth on Ni substrate. CVD: chemical vapor deposition, PECVD: plasma-enhanced CVD and MPCVD: microwave plasma CVD.

Method	Thickness (μm)	Growth Temperature (K)	Slow Cooling Rate (K/s)	Medium Cooling Rate (K/s)	Fast Cooling Rate (K/s)	Ref.
CVD	0.3	1273	-	10.0	-	[S1]
CVD	0.3	1123-1273	0.03	0.07	0.1	[S2]
CVD	0.3	1273	0.1	-	-	[S3]
PECVD	0.5	473-1073	0.1	0.3	0.4	[S4]
CVD	5	1273	0.5	0.4	1.7	[S5]
CVD	5	1173	0.3	-	34.0	[S6]
CVD	25	1273	-	3.3	-	[S7]
CVD	30	1173	0.3	-	3.0	[S8]
CVD	50	1123-1223	-	10.0	-	[S9]
MPCVD	50	723-1023	-	3.0	-	[S10]
CVD	500	973-1273	-	2.7	-	[S11]
CVD	500	1273	0.1	10.0	20.0	[S12]

2   Emission Spectrum Fitting to Estimate the Foil Temperature in the Plasma Region

Figure S-1 shows emission spectra collected by optical emission spectroscopy (OES) from the foil's position in the plasma region. The spectra in Fig. S-1 represents:

(1) the raw emission signal (Emission Spectrum) that was measured by OES after subtracting the baseline offset,

(2) the emission signal after filtering the spectrum from the plasma species (Filtered Emission Spectrum), and

(3) the fitted spectrum using Planck's distribution (Fitted Spectrum) for three temperatures which are 1115, 1100 and 1085 K.

The narrow-spectral emission from plasma species was filtered out using the medfilt1 function in Matlab. Only the baseline of the raw emission spectrum remains unchanged after applying the filter as shown in Fig. S-1. Finally, the filtered baseline is fitted with Planck's distribution (see Eq. 1 in the main paper) to determine the constants (A and B) and the temperature (T) using the nlinfit function in Matlab. The linear offset factor (A) for both Cu and Ni foils takes values between 100 and 250 a.u., depending on web speed and position. However, the factor B remains constant at 5×10^9 and 18.75×10^9 for Cu and Ni, respectively, due to the difference in their emissivities. As a result, the temperature (T), which becomes the only unknown, is derived from the fitting with uncertainty of approximately $\pm$ 15 K as shown by the dashed bounding curves in Fig. S-1.

3   Estimation of the Gas Temperature in the Plasma Region ($T_{\infty 2}$)

The plasma gas temperature ($T_{\infty 2}$) was estimated from the rotational temperature of the Q-branch in the Fulcher band of H_2 in the range of 601-608 nm. Figure S-2 shows the H_2 spectrum and the four lines used to estimate the rotational
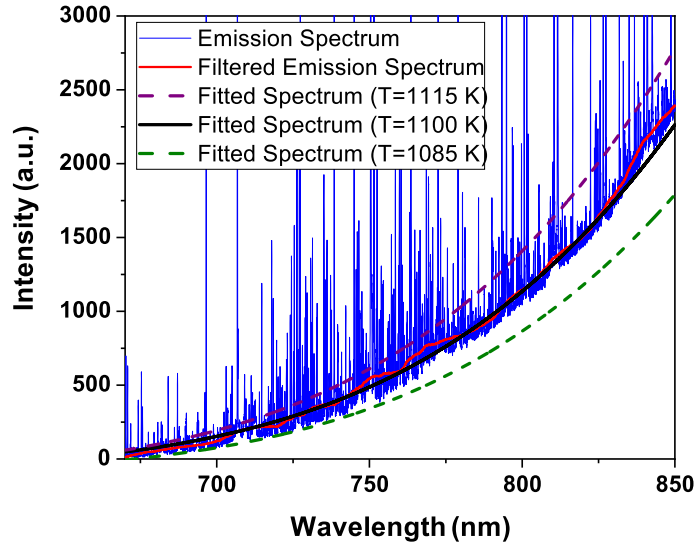
Fig. S-1: Illustration of fitting the emission spectrum to determine the substrate temperature (T) in the plasma region. The noise from the raw emission spectrum (Emission Spectrum) is filtered out to yield the baseline spectrum (Filtered Emission Spectrum), which is fitted with Planck's distribution to find the foil temperature as shown in the Fitted Spectra. The fitted temperature is 1100 K ± 15 K for Cu foil at null speed and a position of 0.49 m.

temperature of H_2. The lines Q_1, Q_2, Q_4 and Q_6 are located at wavelengths (λ) of 601.83, 602.38, 604.27 and 607.20 nm, respectively. A Boltzmann plot, which is presented in the inset of Fig. S-2, was used to infer the rotational temperature from the emission spectrum by analyzing the values of $\ln\left(\frac{I\lambda^4}{S_{J'J''}}\right)$ vs. the rotational energies of the upper state ($E_{J'}$). The values of wavelengths (λ), Hönl-London factors ($S_{J'J''}$) and rotational energies of the upper state ($E_{J'}$) were taken from Ref. [S13]. Also, I is the emission intensity of each line obtained from the spectrum in Fig. S-2. The estimated rotational temperature of H_2 from the Boltzmann plot is 1100 K which is assumed to be in local thermal equilibrium with the plasma gas temperature [S14]. The uncertainty of the gas temperature is about 10 %. The plasma gas temperature ($T_{\infty2}$) was raised to 1140 K for Cu foil at 0 mm/min (instead of 1100 K which is within the measurement uncertainty of 10%) for fitting the numerical model to the foil experimental temperatures.

4 Determination of Convective Heat Transfer Coefficients (h_1, h_2 and h_3)

The heat transfer coefficients in the three regions (h_1, h_2 and h_3) play crucial roles in determining the temperature distribution of the foil. The values of h_1, h_2 and h_3 were derived from fitting the temperature profile of the numerical model to the measured foil temperatures because of the complex fluid flow in the plasma. For this reason, the Cu foil temperatures were measured along the plasma region as shown in Fig. S-3. The measured foil temperatures were compared to the temperature profiles from the numerical model with different values of h_1 and h_3 as presented in Fig. S-3(a). The higher the value of h_1 and h_3, the lower the foil temperatures in the pre- and post-plasma regions, respectively, due to enhanced cooling from the lower temperature gas in these regions. Therefore, h_1 and h_3 are estimated to be 5 W/m^{2}K, although this value is a coarse estimate based on a best fit to limited data in the plasma region as shown in Fig. S-3(a). We further assume that h_1 and h_3 are independent of web speed and foil type; thus h_1 and h_3 remain constant at 5 W/m^{2}K for all cases in this work.

Similarly, the heat transfer coefficient in the plasma region (h_2) was estimated from fitting the temperature profile of the numerical model to the measured Cu foil temperatures in the plasma, as shown in Fig. S-3(b). The Cu foil temperature increases with increased h_2, and has the best fit at 55 W/m^{2}K, which is higher than the convective heat transfer coefficients in the other regions due to intense heating from the energetic plasma. Hence, h_2 is used as a fitting parameter for the numerical model at different web speeds for Cu and Ni foils. Unlike the values of h_1 and h_3 which are assumed to be independent of web speed, the value of h_2 was determined from fitting the spectra at different web speeds for both Cu and Ni foils (refer to Fig. 3 in the main paper). Hence, the best-fit values in increments of 5 W/m^{2}K of h_2 are 55, 30 and 29 W/m^{2}K for Cu at 0, 50 and 150 mm/min, respectively. Also, the values of h_2 for Ni are 36, 30 and 28 W/m^{2}K at 0, 50 and 150 mm/min, respectively. A sensitivity analysis is discussed in Section 6 below to determine the influence of the main input parameters (including h_2) on the model.
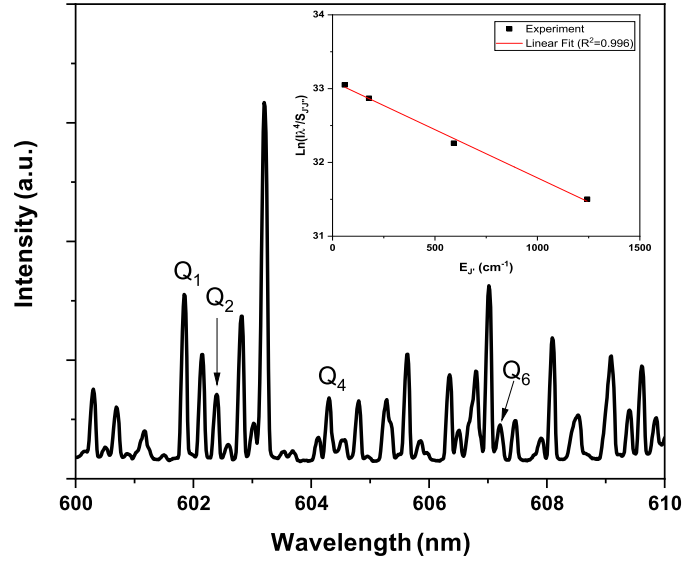
Fig. S-2: The emission spectrum of H_2 Fulcher band showing the 4 Q-branch lines used to estimate the rotational temperature of H_2. The Boltzmann plot is shown in the inset.

5 Derivation of the Heat Transfer Models

Figure S-4 shows a schematic of the foil during the roll-to-roll process. The foil, which has a length of 1 m, is divided into three regions: pre-plasma, plasma and post-plasma. The length of the plasma region, which is denoted as L, equals 12.5 cm. The lengths of the pre-plasma and post-plasma regions are similar and equal 43.75 cm. A control volume in the post-plasma region is shown Fig. S-4. The temperature distribution of the foil is solved both analytically and numerically as explained in the following subsections.

5.1 Derivation of the Analytical Model

The y-coordinate in the analytical model starts from $y^* = y - 0.4375$ m as shown in Fig. S-4 to simplify the solution. Applying an energy balance in the control volume within the post-plasma region results in Eq. 2 in the main paper, which is:

$$q_{y^*} - q_{y^*+dy^*} + w\delta(\rho U c_P T)_{y^*} - w\delta(\rho U c_P T)_{y^*+dy^*} - 2dq_{conv} - dq_{rad,R} - dq_{rad,L} = 0 \tag{S-1}$$

The heat transfer processes in Eq. S-1 represent: axial conduction ($q_{y^*} - q_{y^*+dy^*}$), advection due to the moving foil ($w\delta(\rho U c_P T)_{y^*} - w\delta(\rho U c_P T)_{y^*+dy^*}$), convection from both sides of the foil to the ambient gas ($2dq_{conv}$), and radiation from the right and left sides of the foil to the chamber wall ($dq_{rad,R}$ and $dq_{rad,L}$, respectively). Applying a Taylor expansion for the heat conduction term results in:

$$q_{y^*} - q_{y^*+dy^*} = q_{y^*} - \left(q_{y^*} + \frac{dq_{y^*}}{dy^*}(dy^*)\right) = -\frac{dq_{y^*}}{dy^*}(dy^*) \tag{S-2}$$

Here, (dy^*) is the length of the differential element in the control volume (Fig. S-4). Applying Fourier's law to the conduction term in Eq. S-2 yields:

$$-\frac{dq_{y^*}}{dy^*}(dy^*) = -\left(\frac{d}{dy^*}\left(-wk\delta\frac{dT}{dy^*}\right)\right)(dy^*) = wk\delta(dy^*)\frac{d^2T}{(dy^*)^2} \tag{S-3}$$

where δ is the foil thickness, w is the foil width and k is the thermal conductivity of the foil. Similarly, applying a Taylor expansion for the advection term yields:

$$w\delta(\rho U c_P T)_{y^*} - w\delta(\rho U c_P T)_{y^*+dy^*} = w\delta\rho U c_P T_{y^*} - w\delta\rho U\left(c_P T_{y^*} + \frac{d(c_P T)}{dy^*}(dy^*)\right) = -w\delta\rho U c_P(dy^*)\frac{dT}{dy^*} \tag{S-4}$$
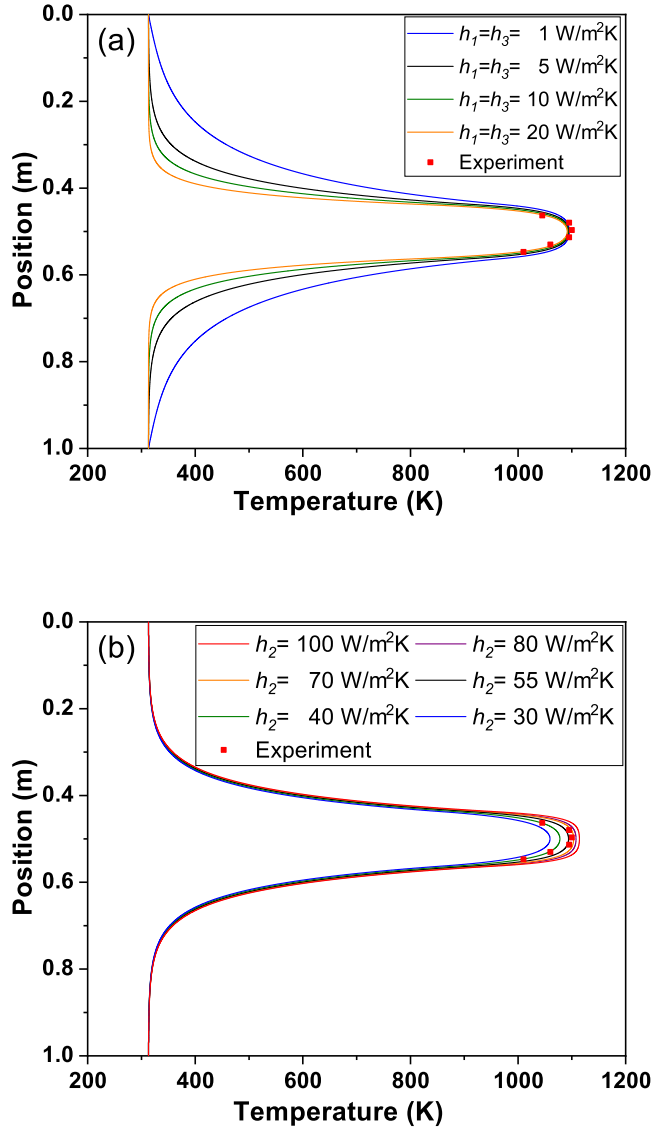
S3

Fig. S-3: The estimation of (a) h_1 and h_3, and (b) h_2 from comparing the Cu foil temperature profiles to the measured temperatures at 850 W power and null web speed (i.e., web speed of 0 mm/min).

where ρ is the density of the foil, U is the web speed and c_P is the specific heat of the foil. We expand the convective (dq_{conv}) and radiative ($dq_{rad,R}$ and $dq_{rad,L}$) terms as follows:

$$dq_{conv} = (dy^*)wh_3(T - T_{\infty 3}) \tag{S-5}$$

$$dq_{rad,R} = (dy^*)w\varepsilon\sigma(T^4 - T_{surr}^4) = (dy^*)w\varepsilon\sigma(T^2 + T_{surr}^2)(T + T_{surr})(T - T_{surr}) = (dy^*)wh_{rad,R3}(T - T_{surr}) \tag{S-6}$$

where $T_{\infty 3}$ is the gas temperature in the post-plasma region, h_3 is the convective heat transfer coefficient in the post-plasma region, and $h_{rad,R3}$ is the linearized radiative heat transfer coefficient written as $h_{rad,R3} = \varepsilon\sigma(T^2 + T_{surr}^2)(T + T_{surr})$ which is similar to the linearized radiative heat transfer coefficient of the other side of the foil (i.e., $h_{rad,L3}$). The temperature of the chamber wall (T_{surr}) is assumed to equal the gas temperature in the post-plasma region (i.e., $T_{\infty 3}$). Finally, ε and σ are the emissivity of the foil and the Stefan-Boltzmann constant, respectively. Combining the terms in Eqs. S-3, S-4, S-5 and S-6,
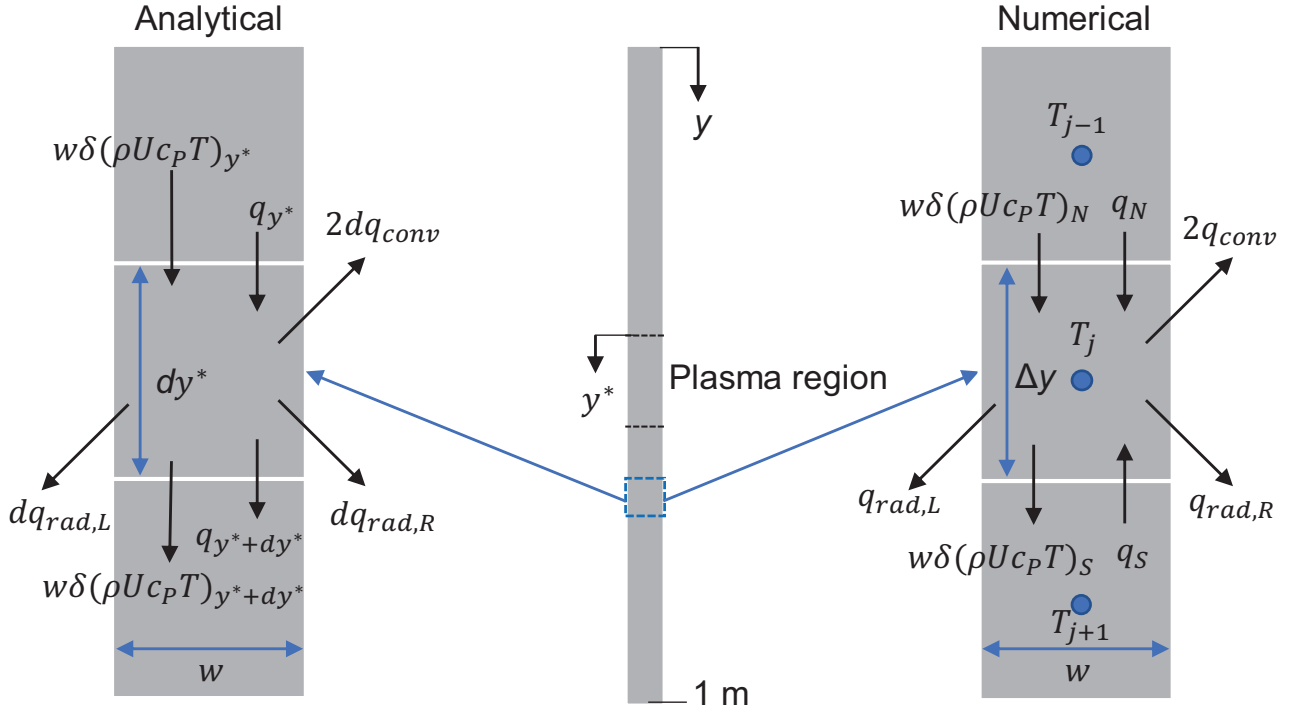
Fig. S-4: Schematic of the foil undergoing graphene growth in the roll-to-roll plasma CVD system. The plasma region starts at $y = 0.4375$ m (but at $y^* = y - 0.4375$ m in the analytical model). The modeling domain of the foil starts from the top spool and ends at the bottom spool as shown in Fig. 1 in the main paper.

the final form of the differential equation corresponding to Eq. S-1 (or Eq. 2 in the main paper) becomes:

$$wk\delta(dy^*)\frac{d^2T}{(dy^*)^2} - w\delta\rho Uc_P(dy^*)\frac{dT}{dy^*} - 2(dy^*)wh_3(T - T_{\infty 3}) - 2(dy^*)wh_{rad,R3}(T - T_{\infty 3}) = 0 \tag{S-7}$$

Dividing Eq. S-7 by $(wk\delta(dy^*))$ yields:

$$\frac{d^2T}{(dy^*)^2} - \frac{\rho Uc_P}{k}\frac{dT}{dy^*} - \frac{2h_3}{k\delta}(T - T_{\infty 3}) - \frac{2h_{rad,R3}}{k\delta}(T - T_{\infty 3}) = 0 \tag{S-8}$$

Letting $\theta_3 = (T - T_{\infty 3})$, $a = \frac{\rho Uc_P}{k}$ and $m_3 = \frac{2h_3}{k\delta} + \frac{2h_{rad,R3}}{k\delta}$, the final differential equation is:

$$\frac{d^2\theta_3}{(dy^*)^2} - a\frac{d\theta_3}{dy^*} - m_3\theta_3 = 0 \tag{S-9}$$

5.1.1   Radiation Heat Transfer in the Plasma Region in the Analytical Model

Radiation heat transfer from the foil to the electrodes in the plasma region is linearized in the analytical model to simplify the solution. The linearized radiation heat transfer coefficient from the foil to the right electrode, for example, is determined by employing the radiation resistance network [S15]:

$$dq_{rad,RE} = \frac{w(dy^*)\sigma(T^2 + T_{RE}^2)(T + T_{RE})}{\frac{1-\varepsilon}{\varepsilon} + \frac{1-\varepsilon_E}{\varepsilon_E}\frac{dy^*}{L} + \frac{1}{F_{foil-RE}}}(T - T_{RE}) \tag{S-10}$$

where T_{RE} is the temperature of the right electrode and L is the length of the electrode. The view factor ($F_{foil-RE}$) and the emissivity of foil (ε) are obtained from [S15]. The graphite electrode (emissivity, ε_E) is assumed to be a blackbody. Thus, we

can write the linearized radiative heat transfer coefficient due to the radiation exchange between foil and the right electrode as:

$$h_{rad,RE} = \frac{\sigma(T^2 + T_{RE}^2)(T + T_{RE})}{\frac{1-\varepsilon}{\varepsilon} + \frac{1}{F_{foil-RE}}} \tag{S-11}$$

The first and second terms in the denominator represent the foil surface resistance and the space resistance, respectively. A similar formula is obtained for radiation transfer between the foil and the left electrode.

Furthermore, the radiation exchange between the foil and the chamber wall is neglected in the heat transfer analysis of the foil in the plasma region to achieve a closed form of solution in terms of $\theta_2 = (T - T_{\infty 2})$. Hence, the temperature of the electrodes (T_{RE} and T_{LE}) is assumed to be equal to $T_{\infty 2}$. These simplifications are applied only in the analytical model to combine the convective and radiative terms in m_2 and to simplify the differential equation, which is written as:

$$\frac{d^2\theta_2}{(dy^*)^2} - a\frac{d\theta_2}{dy^*} - m_2\theta_2 = 0 \tag{S-12}$$

where $\theta_2 = (T - T_{\infty 2})$, $a = \frac{\rho U c_P}{k}$ and $m_2 = \frac{2h_2}{k\delta} + \frac{h_{rad,R2}}{k\delta} + \frac{h_{rad,L2}}{k\delta}$. Here, $h_{rad,R2} = h_{rad,RE}$ from Eq. S-11 and the value of h_2 is derived by fitting the model to the measured foil temperatures as discussed in the main paper and shown in Fig. S-3(b) above.

5.1.2 The Constants (C_2, C_3, C_5 and C_6) in the Analytical Model

The linear equations from the boundary conditions (c)-(f) in the main paper were solved algebraically to find the constants (C_2, C_3, C_5 and C_6) in Eq. 6 in the main paper which take the forms:

$$C_2 = \frac{e_4((k_2^2 r_5 r_6 - r_5 e_5 e_6 (k_2^2 r_6 + k_1 k_2 r_1))(T_{\infty 3} - T_{\infty 2}) + k_1 k_2 r_1 r_5 e_5 (T_{\infty 1} - T_{\infty 2}))}{-k_2^2 r_5 r_6 (1 - e_5 e_6) + k_1 r_1 (k_2 r_6 - k_3 r_4) + k_2 k_3 r_4 r_5 + e_5 e_6 (k_1 k_3 r_1 r_4 + k_1 k_2 r_1 r_5 + k_2 k_3 r_4 r_6)} \tag{S-13}$$

$$C_3 = \frac{k_2^2 r_5 r_6 (T_{\infty 1} - T_{\infty 2})(1 - e_5 e_6) - k_3 k_2 r_4 (T_{\infty 1} - T_{\infty 2})(r_5 + r_6 e_5 e_6) + k_3 k_2 r_4 e_6 (T_{\infty 3} - T_{\infty 2})(r_5 - r_6)}{-k_2^2 r_5 r_6 (1 - e_5 e_6) + k_1 r_1 (k_2 r_6 - k_3 r_4) + k_2 k_3 r_4 r_5 + e_5 e_6 (k_1 k_3 r_1 r_4 + k_1 k_2 r_1 r_5 + k_2 k_3 r_4 r_6)} \tag{S-14}$$

$$C_5 = \frac{k_1 r_1 (k_2 r_6 - k_3 r_4)(T_{\infty 1} - T_{\infty 2}) + k_3 r_4 e_6 (k_1 r_1 + k_2 r_6)(T_{\infty 3} - T_{\infty 2})}{-k_2^2 r_5 r_6 (1 - e_5 e_6) + k_1 r_1 (k_2 r_6 - k_3 r_4) + k_2 k_3 r_4 r_5 + e_5 e_6 (k_1 k_3 r_1 r_4 + k_1 k_2 r_1 r_5 + k_2 k_3 r_4 r_6)} \tag{S-15}$$

$$C_6 = \frac{e_6 (k_3 r_4 (k_2 r_5 - k_1 r_1)(T_{\infty 3} - T_{\infty 2}) + k_1 r_1 e_5 (k_3 r_4 + k_2 r_5)(T_{\infty 1} - T_{\infty 2}))}{-k_2^2 r_5 r_6 (1 - e_5 e_6) + k_1 r_1 (k_2 r_6 - k_3 r_4) + k_2 k_3 r_4 r_5 + e_5 e_6 (k_1 k_3 r_1 r_4 + k_1 k_2 r_1 r_5 + k_2 k_3 r_4 r_6)} \tag{S-16}$$

where: $e_4 = \exp(\frac{Lr_4}{2})$, $e_5 = \exp(\frac{Lr_5}{2})$, $e_6 = \exp(\frac{Lr_6}{2})$, $r_1 = \sqrt{a^2 + 4m_1} + a$, $r_4 = \sqrt{a^2 + 4m_3} - a$, $r_5 = \sqrt{a^2 + 4m_2} + a$, $r_6 = \sqrt{a^2 + 4m_2} - a$, $a = \frac{\rho U c_P}{k}$, $m_1 = \frac{2h_1}{k\delta} + \frac{2h_{rad,R1}}{k\delta}$, $m_2 = \frac{2h_2}{k\delta} + \frac{h_{rad,R2}}{k\delta} + \frac{h_{rad,L2}}{k\delta}$ and $m_3 = \frac{2h_3}{k\delta} + \frac{2h_{rad,R3}}{k\delta}$. Also, k_1, k_2 and k_3 represent the foil thermal conductivity in the pre-plasma, plasma and post-plasma regions, respectively. In addition, $T_{\infty 1}$, $T_{\infty 2}$ and $T_{\infty 3}$ are the gas temperatures in the pre-plasma, plasma and post-plasma regions, respectively.

5.2 Derivation of the Numerical Model

The temperature distribution of the foil was also solved numerically in order to incorporate non-linearities in the radiation heat transfer and temperature-dependent material properties. The energy balance in the control volume of the foil in Fig. S-4 accounts for conduction (q_N and q_S), advection ($w\delta\rho U c_P T_N$ and $w\delta\rho U c_P T_S$), convection (q_{conv}), and radiation ($q_{rad,R}$ and $q_{rad,L}$). The discretization of conduction, advection and convection terms are included in the main paper. The discretization of the radiation exchange between the foil and surroundings (chamber wall and electrodes) is explained below.

Radiation exchange from the foil to the right electrode and the chamber wall ($q_{rad,R}$), for example, is written in terms of the space resistance as [S15]:

$$q_{rad,R} = \frac{E_{b,foil} - J_{foil-R}}{\frac{1-\varepsilon}{\varepsilon(\Delta y)w}} \tag{S-17}$$

where: $E_{b,foil} = \sigma T_j^4$, and the radiosity J_{foil-R} is obtained from the previous iteration (i.e., J_{foil-R}^*). Thus, the radiation term of Eq. S-17 can be written as:

$$q_{rad,R} = \frac{\sigma T_j^4 - J_{foil-R}}{\frac{1-\varepsilon}{\varepsilon(\Delta y)w}} = \frac{\varepsilon(\Delta y)w(\sigma T_j^4 - J_{foil-R}^*)}{1-\varepsilon} = \frac{\varepsilon(\Delta y)w\sigma T_j^4}{1-\varepsilon} - \frac{\varepsilon(\Delta y)wJ_{foil-R}^*}{1-\varepsilon} \tag{S-18}$$

The first term on the right side of Eq. S-18 is treated as follows [S16]:

$$\frac{\varepsilon(\Delta y)w\sigma T_j^4}{1-\varepsilon} = \frac{\varepsilon(\Delta y)w\sigma(T_j^*)^4}{1-\varepsilon} + \left(\frac{4\varepsilon(\Delta y)w\sigma(T_j^*)^3}{1-\varepsilon}(T_j - T_j^*)\right) = \frac{4\varepsilon(\Delta y)w\sigma(T_j^*)^3}{1-\varepsilon}T_j - \frac{3\varepsilon(\Delta y)w\sigma(T_j^*)^4}{1-\varepsilon} \tag{S-19}$$

where T_j^* is the temperature of cell "j" from the previous iteration. The radiation term becomes:

$$q_{rad,R} = \frac{4\varepsilon(\Delta y)w\sigma(T_j^*)^3}{1-\varepsilon}T_j - \frac{\varepsilon(\Delta y)w(J_{foil-R}^* + 3\sigma(T_j^*)^4)}{1-\varepsilon} \tag{S-20}$$

We find J_{foil-R}^* by forming a radiation resistance network using the radiosity of the right side of foil to the right electrode (J_{RE}) and the radiosity of the chamber wall ($J_W = \varepsilon_W \sigma T_W^4$) [S15]:

$$\frac{E_{b,foil} - J_{foil-R}}{\frac{1-\varepsilon}{\varepsilon A_{foil}}} = \frac{J_{foil-R} - J_{RE}}{\frac{1}{A_{foil}F_{foil-RE}}} + \frac{J_{foil-R} - J_W}{\frac{1}{A_{foil}F_{foil-W}}} \tag{S-21}$$

The view factor ($F_{foil-RE}$) is determined using a differential planar element to a finite parallel rectangle [S17]. Using the summation rule, we write $F_{foil-W} = 1 - F_{foil-RE}$. Here, ε_W is the emissivity of the chamber wall (assumed to equal 1.0 due to significant carbonization from previous experiments), whereas the emissivity of Ni and Cu are 0.14 and 0.04, respectively, at 1000 K. T_W is the temperature of the chamber wall which is assumed to equal $T_{\infty 1}$ and $T_{\infty 3}$ (i.e., 313 K). Therefore, the radiosity is found from the previous iteration as [S16]:

$$a_{foil}J_{foil-R}^* = a_{foil-RE}J_{foil-RE}^* + a_{foil-W}J_{foil-W}^* + \frac{\varepsilon(\Delta y)w}{1-\varepsilon}\sigma(T_j^*)^4 \tag{S-22}$$

$$a_{foil} = a_{foil-RE} + a_{foil-W} + \frac{\varepsilon(\Delta y)w}{1-\varepsilon}$$

$$a_{foil-RE} = (\Delta y)wF_{foil-RE}$$

$$a_{foil-W} = (\Delta y)wF_{foil-W}$$

A similar derivation can be performed for the radiation from the substrate to the left electrode, which results in similar equations.

5.2.1 Mesh-independence Study for the Numerical Model

A mesh-independence study led to a cell size (Δy) of 10^{-4} m (i.e., the number of cells is 10,000) as shown in Fig. S-5. The temperature distributions of the foil when $\Delta y = 10^{-4}$ m and $\Delta y = 10^{-5}$ m are equal. Thus, the mesh size of $\Delta y = 10^{-4}$ m was used in this work to reduce computational time.
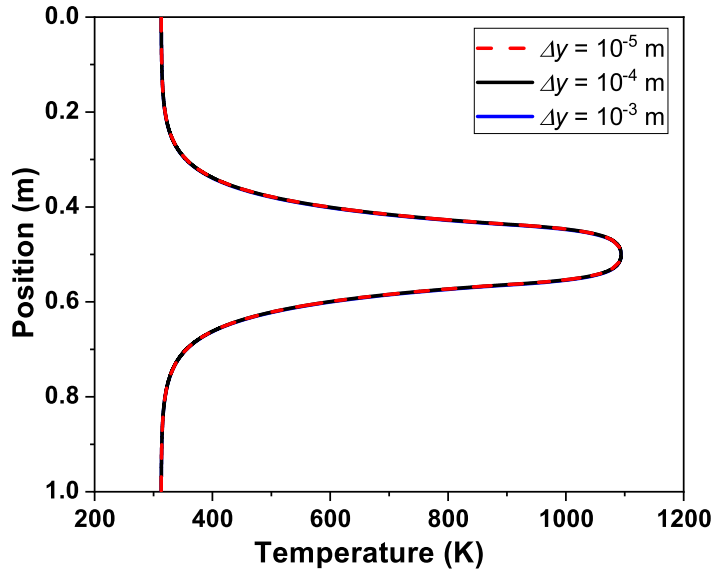
Fig. S-5: Mesh independence study with different cell sizes (Δy) in the numerical model. The results with cell sizes (Δy) of 10^{-4} and 10^{-5} m are similar. Thus, the cell size of $\Delta y = 10^{-4}$ m is used in this study. The plasma power for this case is 850 W at 0 mm/min with Cu foil.

5.3 Comparison Between the Analytical and Numerical Models

Predicted temperature distributions of Cu foil from the analytical and numerical models are presented in Fig. S-6. The plasma power and web speed in the results of Fig. S-6 are 850 W and 0 mm/min, respectively. Both analytical and numerical models have identical temperature profiles when the radiation heat transfer is neglected. The inclusion of radiation in the analytical model raises the maximum temperature slightly. However, the maximum Cu foil temperature decreases by approximately 39 K when including the radiation terms in the numerical model. This temperature drop is attributed to heat loss by radiation from the high-temperature substrate to the lower-temperature chamber wall and electrodes [S18]. Due to the simplifications made in the analytical model to linearize the radiation terms in order to obtain a closed-form solution of foil temperature, the analytical model is used to qualitatively clarify the trends of the foil temperature with variations in process conditions. On the other hand, the numerical model with radiation heat transfer (referred as the numerical model through this work) is used to derive the actual substrate temperature distribution and the rate of temperature change.

6 Sensitivity Analysis

A sensitivity analysis is made to determine the influence of the main input parameters on the model. The uncertainty bands of input parameters, based on measurements uncertainty or assumption, are listed in Table S-2. The normalized sensitivity coefficient is defined as [S19]:

$$Sensitivity\ Coefficient = \frac{\partial T}{\partial P_i}\left(\frac{P_i}{T}\right) \tag{S-23}$$

where (T) and (P_i) are the foil temperature and an input parameter, respectively. Assuming a linear sensitivity correlation between temperature and each parameter [S19, S20], the normalized sensitivity coefficient can be approximated as:

$$Sensitivity\ Coefficient \approx \frac{(T_H - T_L)/T_B}{(P_{iH} - P_{iL})/P_{iB}} \tag{S-24}$$

where T_H, T_B, and T_L are the maximum temperatures in the plasma region using the high (P_{iH}), best-fit (P_{iB}) and low (P_{iL}) values of a parameter (P_i), respectively. Only one factor was changed at a time while the other input parameters are fixed at
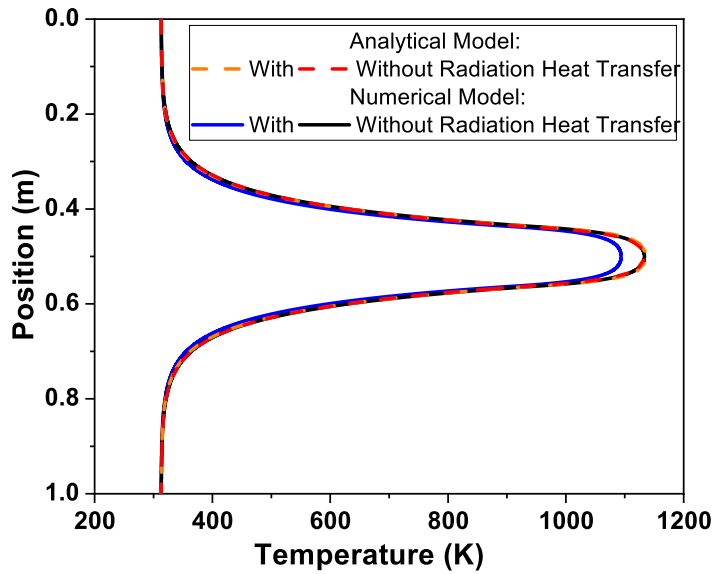
Fig. S-6: Comparison between the Cu foil temperature distributions from the analytical and numerical models (with and without radiation heat transfer) at 850 W and 0 mm/min

the best-fit values listed in Table S-2. Figure S-7 presents sensitivity coefficients of the main input parameters on the model for Cu and Ni foils at 50 mm/min. The model is more sensitive to changes in plasma gas temperature ($T_{\infty 2}$), followed by the electrode temperatures (T_{RE} and T_{LE} for the right and left electrodes, respectively), the heat transfer coefficient in the plasma region (h_2) and the foil emissivity (ε). The gas temperature in the pre-plasma region ($T_{\infty 1}$), heat transfer coefficient in the pre-plasma region (h_1), and velocity (U) have negligible sensitivity coefficients. The sensitivity coefficients of the input parameters on the model for Cu and Ni foils at 0 and 150 mm/min have similar ranges of values to the results at 50 mm/min.

The plasma gas temperature ($T_{\infty 2}$), the electrode temperatures (T_{RE} and T_{LE}) and the heat transfer coefficient in the plasma region (h_2) have a positive sensitivity coefficient that indicates an increased temperature prediction with increased of these parameters. The foil temperature increases with the plasma gas temperature ($T_{\infty 2}$) and the heat transfer coefficient in the plasma region (h_2) due to enhanced convection heat transfer from the high-temperature plasma gas. The foil temperature increases with the electrode temperatures (T_{RE} and T_{LE}) due to lower radiation exchange between the foil and the electrodes. However, the emissivity has a negative sensitivity coefficient that indicates a reduced foil temperature with increased emissivity because of increased radiation exchange between the high foil temperature to the low temperature electrodes and chamber wall.

The model is more sensitive to the convective heat transfer conditions (i.e., $T_{\infty 2}$ and h_2) than radiation heat transfer (i.e., T_{RE}, T_{LE} and ε). The sensitivity coefficients of $T_{\infty 2}$ and h_2 are higher for Cu than Ni because of higher thermal conductivity for the former. On the other hand, the sensitivity coefficients of T_{RE}, T_{LE} and ε are higher for Ni than Cu because of a higher emissivity of Ni than Cu. The sensitivity coefficient of T_{surr} is negligible because of lower foil temperature in the pre- and post-plasma regions for both Ni and Cu. Also, the view factor between the foil and the chamber wall is reduced in the plasma region. Hence, the sensitivity coefficient of T_{surr} on the model is negligible.

In addition, the temperature distributions for Ni foil at 50 mm/min at the minimum, best-fit, and maximum values of the most sensitivity coefficients are included in Fig. S-8. These results show that the model has lower sensitivity on the heat transfer coefficient compared to the plasma gas temperature and the electrode temperatures as shown in Fig. S-7. Also, the inset in each figure of Fig. S-8 shows the linear fit between the temperature and the corresponding input parameter.

Table S-2: Uncertainty bands of input parameters for Cu and Ni foils at 50 mm/min web speed

| Parameter (P)	Uncertainty	Low value (P_L)	best-fit value (P_B)	High value (P_L)
Temperature in the plasma region ($T_{\infty 2}$), [K]	10%	990	1100	1210
Temperature in the pre-plasma region ($T_{\infty 1}$), [K]	10%	297	313	329
Temperature of the right electrode (T_{RE}), [K]	5%	847	892	937
Temperature of the left electrode (T_{LE}), [K]	5%	827	870	914
Web speed (U), [mm/min]	10%	45	50	55
The heat transfer coefficient in the plasma region (h_2), [W/m^{2}K]	Best fit to the foil temperature measurements	Cu: 17, Ni: 17	Cu: 30, Ni: 30	Cu: 60, Ni: 55
The heat transfer coefficient in the pre-plasma region (h_1), [W/m^{2}K]	Best fit to the foil temperature measurements	1	5	10
Emissivity (ε), [-]	Assumption	Cu: 0.03, Ni: 0.13	Cu: 0.04, Ni: 0.14	Cu: 0.05, Ni: 0.15
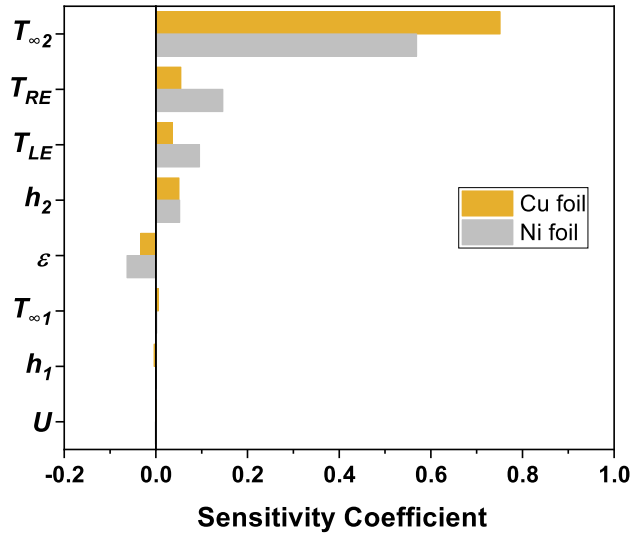
Fig. S-7: Sensitivity analysis to the temperature distribution from the model for various input parameters for Cu and Ni foils at 50 mm/min
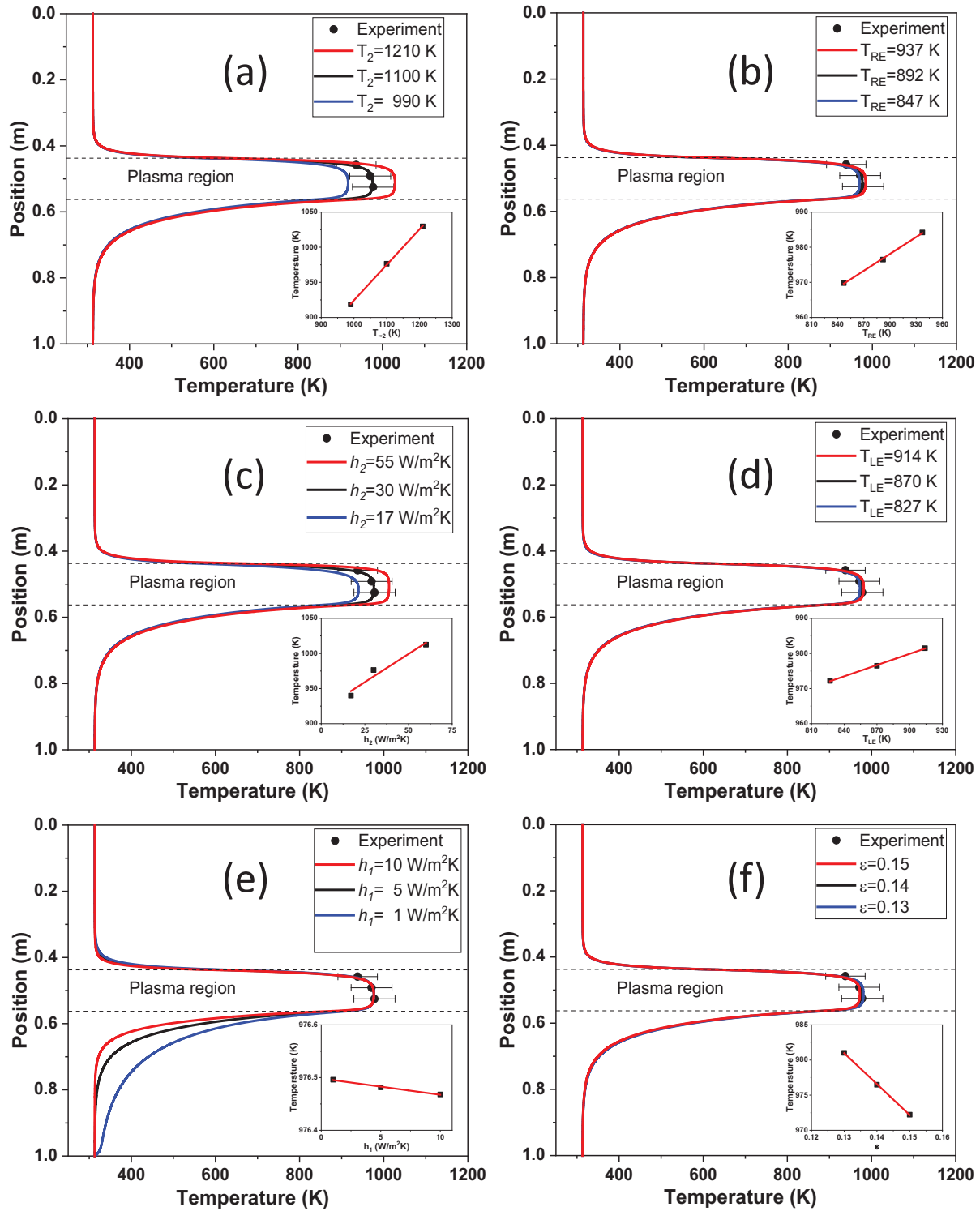
Fig. S-8: Effects of input parameters on the temperature distribution of Ni foil at 50 mm/min. (a) Temperature in the plasma region ($T_{\infty 2}$). (b) Temperature of the right electrode (T_{RE}). (c) Heat transfer coefficient in the plasma region (h_2). (d) Temperature of the left electrode (T_{LE}). (e) Heat transfer coefficient in the pre-plasma region (h_1). (f) Foil emissivity (ε). The inset in each figure shows the linear fit between the temperature and the corresponding input parameter.

References

[S1] Kim, K. S., Zhao, Y., Jang, H., Lee, S. Y., Kim, J. M., Kim, K. S., Ahn, J.-H., Kim, P., Choi, J.-Y., and Hong, B. H., 2009. "Large-scale pattern growth of graphene films for stretchable transparent electrodes". *Nature,* **457**(7230), pp. 706–710.

[S2] Lee, B.-J., Yu, H.-Y., and Jeong, G.-H., 2010. "Controlled synthesis of monolayer graphene toward transparent flexible conductive film application". *Nanoscale research letters,* **5**(11), pp. 1768–1773.

[S3] Park, H. J., Meyer, J., Roth, S., and Skákalová, V., 2010. "Growth and properties of few-layer graphene prepared by chemical vapor deposition". *Carbon,* **48**(4), pp. 1088–1094.

[S4] Cheng, L., Yun, K., Lucero, A., Huang, J., Meng, X., Lian, G., Nam, H.-S., Wallace, R. M., Kim, M., Venugopal, A., et al., 2015. "Low temperature synthesis of graphite on ni films using inductively coupled plasma enhanced cvd". *Journal of Materials Chemistry C,* **3**(20), pp. 5192–5198.

[S5] Reina, A., Thiele, S., Jia, X., Bhaviripudi, S., Dresselhaus, M. S., Schaefer, J. A., and Kong, J., 2009. "Growth of large-area single-and bi-layer graphene by controlled carbon precipitation on polycrystalline ni surfaces". *Nano Research,* **2**(6), pp. 509–516.

[S6] Miyata, Y., Kamon, K., Ohashi, K., Kitaura, R., Yoshimura, M., and Shinohara, H., 2010. "A simple alcohol-chemical vapor deposition synthesis of single-layer graphenes using flash cooling". *Applied Physics Letters,* **96**(26), p. 263105.

[S7] Huang, L., Chang, Q., Guo, G., Liu, Y., Xie, Y., Wang, T., Ling, B., and Yang, H., 2012. "Synthesis of high-quality graphene films on nickel foils by rapid thermal chemical vapor deposition". *Carbon,* **50**(2), pp. 551–556.

[S8] Juang, Z.-Y., Wu, C.-Y., Lu, A.-Y., Su, C.-Y., Leou, K.-C., Chen, F.-R., and Tsai, C.-H., 2010. "Graphene synthesis by chemical vapor deposition and transfer by a roll-to-roll process". *Carbon,* **48**(11), pp. 3169–3174.

[S9] Cai, W., Zhu, Y., Li, X., Piner, R. D., and Ruoff, R. S., 2009. "Large area few-layer graphene/graphite films as transparent thin conducting electrodes". *Applied Physics Letters,* **95**(12), p. 123115.

[S10] Kim, Y., Song, W., Lee, S., Jeon, C., Jung, W., Kim, M., and Park, C.-Y., 2011. "Low-temperature synthesis of graphene on nickel foil by microwave plasma chemical vapor deposition". *Applied Physics Letters,* **98**(26), p. 263106.

[S11] Chae, S. J., Güneş, F., Kim, K. K., Kim, E. S., Han, G. H., Kim, S. M., Shin, H.-J., Yoon, S.-M., Choi, J.-Y., Park, M. H., et al., 2009. "Synthesis of large-area graphene layers on poly-nickel substrate by chemical vapor deposition: wrinkle formation". *Advanced Materials,* **21**(22), pp. 2328–2333.

[S12] Yu, Q., Lian, J., Siriponglert, S., Li, H., Chen, Y. P., and Pei, S.-S., 2008. "Graphene segregated on ni surfaces and transferred to insulators". *Applied Physics Letters,* **93**(11), p. 113103.

[S13] Shivkumar, G., Tholeti, S., Alrefae, M., Fisher, T., and Alexeenko, A., 2016. "Analysis of hydrogen plasma in a microwave plasma chemical vapor deposition reactor". *Journal of Applied Physics,* **119**(11), p. 113301.

[S14] Shivkumar, G., Alrefae, M., Tholeti, S., Macheret, S., Fisher, T., and Alexeenko, A., 2019. "Discharge regimes and emission characteristics of capacitively coupled radio frequency argon plasma with a square wave input". *Journal of Applied Physics,* **125**(22), p. 223301.

[S15] Bergman, T. L., Incropera, F. P., DeWitt, D. P., and Lavine, A. S., 2011. *Fundamentals of heat and mass transfer.* John Wiley & Sons.

[S16] Murthy, J. Y., 2002. Numerical methods in heat, mass, and momentum transfer. Draft notes, School of Mechanical Engineering, Purdue University.

[S17] Modest, M. F., 2013. *Radiative heat transfer.* Academic press.

[S18] Karwe, M., and Jaluria, Y., 1988. "Fluid flow and mixed convection transport from a moving plate in rolling and extrusion processes". *JOURNAL OF HEAT TRANSFER-TRANSACTIONS OF THE ASME,* **110**(3), pp. 655–661.

[S19] Hamby, D. M., 1994. "A review of techniques for parameter sensitivity analysis of environmental models". *Environmental monitoring and assessment,* **32**(2), pp. 135–154.

[S20] Dowding, K. J., and Blackwell, B. F., 2001. "Sensitivity analysis for nonlinear heat conduction". *JOURNAL OF HEAT TRANSFER-TRANSACTIONS OF THE ASME,* **123**(1), pp. 1–10.